iScience

CellPress
OPEN ACCESS

Review

Contactless Thermometry by MRI and MRS: Advanced Methods for Thermotherapy and Biomaterials

Norbert W. Lutz[1,*] and Monique Bernard[1]

SUMMARY

Control of temperature variation is of primordial importance in particular areas of biomedicine. In this context, medical treatments such as hyperthermia and cryotherapy, and also the development and use of hydrogel-based biomaterials, are of particular concern. To enable accurate temperature measurement without perturbing or even destroying the biological tissue or material to be monitored, contactless thermometry methods are preferred. Among these, the most suitable are based on magnetic resonance imaging and spectroscopy (MRI, MRS). Here, we address the latest developments in this field as well as their current and anticipated practical applications. We highlight recent progress aimed at rendering MR thermometry faster and more reproducible, versatile, and sophisticated and provide our perspective on how these new techniques broaden the range of applications in medical treatments and biomaterial development by enabling insight into finer details of thermal behavior. Thus, these methods facilitate optimization of clinical and industrial heating and cooling protocols.

INTRODUCTION

Temperature variation and control play an important role in biological organisms. Bacteria known as extremophiles, living under extreme environmental conditions previously thought to be unable to maintain life, exist at a very broad range of temperatures: from < −40°C for psychrophiles or cryophiles (Panikov et al., 2006) to >120°C for hyperthermophiles (Madigan et al., 2018; Takai et al., 2008). Thermophiles have optimal growth temperatures of 45°C–70°C (Madigan et al., 2018; Sarhan and Alamrri, 2014). By contrast, animals are typically viable within a much smaller temperature range. In particular mammals require a close regulation of body temperature within a narrow range (36°C–40°C) for normal physiological function (Jessen, 2001), notwithstanding that some mammals tolerate atypically low body temperatures during hibernation, e.g., from just over 30°C for bears to <0°C for the arctic ground squirrel (Barnes, 1989). In humans, conditions such as fever or malignant hyperthermia rarely raise the physiological temperature of 37°C by more than 3°C–4°C (Fauci, 2008). However, there are a number of medical treatment modes that may produce substantially larger temperature variations. For instance, the body temperature of patients undergoing heart surgery may be lowered to <30°C (deep hypothermia) to minimize tissue damage due to ischemia (Saad and Aladawy, 2013). In some patients such as comatose cardiac arrest survivors, targeted temperature management involving hypothermia is employed for neuroprotection (Tong et al., 2019). Donor hearts and other organs to be transplanted are generally stored at temperatures as low as 4°C for protection (Michel et al., 2015). Drastic tissue temperature decreases to < −50°C are caused by cryosurgery (Andrews, 2004; Baust et al., 2014; Clebak et al., 2020). On the other hand, the local tissue temperature may significantly exceed 50°C in particular clinical hyperthermia treatment modes employed in patients suffering from various neurological, cardiologic, and other conditions as well as in selected malignant tumors, especially if rapid tissue ablation is desired (Mueller and Adam, 2012). In this review, any medical treatment method based on tissue temperature alteration is referred to as thermotherapy.

Over the past few decades, rapid progress has been achieved in the development of new biomaterials. Here, hydrogel-based materials are of particular interest as they resemble tissue with respect to their high water content (most soft tissues consist of 70%–80% water, and most hydrogel-based materials are made of >80% water [Savina et al., 2016; Warren et al., 2017]). The production of hydrogels involves heating

[1]Aix-Marseille University, CNRS, CRMBM, 27 Bd Jean Moulin, 13005 Marseille, France

*Correspondence: nlutz@umars.fr

https://doi.org/10.1016/j.isci.2020.101561

of the polymer/water mixture of choice, sol formation upon dissolution of the polymer, and gel formation during subsequent cooling. The quality of the resulting gel depends, among other factors, on temperature control during the cooling process (Ahmed, 2015; Savina et al., 2016). For instance, gel morphology varies with the cooling rate, and the pore size of the gel is critically influenced by the speed of freezing and subsequent defrosting (Savina et al., 2016). Besides the production process also the actual use of a number of hydrogel-based biomaterials may be thermally controlled. For instance, the temperature sensitivity of hydrogels is exploited in applications such as drug delivery, protein delivery, and gene therapy. Recent developments include "smart hydrogels" that are currently extensively investigated as biomaterials to be used in wound covering, as cell carriers, and in the domain of tissue engineering and regenerative medicine aimed at tissue repair (Mantha et al., 2019; Warriner et al., 2014).

To enable accurate temperature measurement without perturbing or even destroying the biological tissue or biomaterial to be monitored, a limited number of contactless thermometry methods have been developed. One of these, based on infrared (IR) light, is extremely precise, fast, efficient, and easy to handle; however, IR can only be used to measure temperature at the surface of objects of interest because IR light does not significantly penetrate tissue and other materials of interest (Chesterton et al., 2002; Mei et al., 2018; Piazena et al., 2019), unless invasive transponders are employed. For this reason, the IR technique is inadequate when thermal processes occurring inside objects are to be characterized. By contrast, methods based on magnetic resonance imaging (MRI) and magnetic resonance spectroscopy (MRS), both based on the nuclear magnetic resonance (NMR) phenomenon, proved to be the most suitable approach for detailed thermal analysis of three-dimensional objects containing large amounts of water, in particular body tissue and hydrogel-based materials. NMR refers to the collective magnetic behavior of nuclear spins (i.e., magnetic moments of atomic nuclei) in a magnetic field, under the action of electromagnetic radiation of an appropriate frequency, the so-called resonance frequency.

MRS and MRI techniques have long been used to measure physicochemical parameters. Although the first widespread MR applications concerned the identification of molecular structures (Proctor and Yu, 1950), dynamic processes such as molecular mobility (Bloembergen et al., 1948), diffusion (Hahn, 1950), and chemical exchange may also affect MR signals, which in turn reflect physicochemical properties of the material under investigation. This feature has been exploited to quantitatively measure physicochemical parameters of samples by way of MR techniques. Among the physicochemical parameters that have been quantified in biomedical MRS and MRI are pH, temperature, and concentrations of different metal ions, and also electric conductivity and permittivity as well as elasticity of tissue. Some of these measurements can be obtained on the basis of MR signals from endogenous compounds, e.g., the proton (^{1}H) resonance from tissue water for temperature measurement with or without addition of contrast agents. Other investigations require detection of MR signals from exogenous reporter molecules that need to be added to the material to be studied. In this review, we will predominantly focus on approaches to thermometry based on the so-called chemical shift, δ, of the water ^{1}H MR resonance. Chemical shift is a measure of the resonance frequency of magnetic nuclei but is normalized to the strength of the magnetic field used, such that δ values become independent of field strength. This group of MR thermometry (MRT) methods, collectively referred to as proton resonance frequency (PRF), has eclipsed all other forms of MR-based thermometry and is likely to dominate the field in the future. Alternative MRT techniques have been reviewed recently, along with an extensive discussion of the basic principles developed several decades ago (Odéen and Parker, 2019a).

In the domain of water ^{1}H MRT techniques, carefully reviewed by Rieke et al. (Rieke and Butts Pauly, 2008), the overwhelming majority of practical (in particular biomedical) applications currently employ variants of one particular approach, viz., chemical shift-based phase imaging of (tissue) water. However, the principle underlying phase-based PRF only permits determination of temperature changes over time, but not of absolute temperature values, as opposed to spectroscopic PRF that can directly measure absolute temperatures. Since nearly all MRT developments of the past 5–10 years were geared toward rendering the phase-based PRF approach more reproducible, versatile, and sophisticated, we particularly emphasize phase imaging methods. Additional technical details are placed in Supplemental Information (Table S1) where this seems beneficial for superior readability of the main text. Many recent improvements reflect the need for fast (real-time) temperature mapping, notably in the context of interventional MRI during thermal tissue ablation. Thus, the combination of tissue heating by high-intensity focused ultrasound (HIFU) and MRT represents a particularly active domain of research (MR guided focused ultrasound, MRgFUS). In this context, much attention has been paid not only to ensuring

adequate heating of tissue areas to be ablated but also to minimizing heating of adjacent, healthy tissue. MRgFUS is an entirely noninvasive method using an external transducer to focus high-power ultrasound into tissue. This technique has been successfully used in humans to treat uterine fibroids, bone metastasis-related pain, cancer, and deep brain tissue (Jonathan and Grissom, 2018); see also Table S1. Apart from tissue ablation, MRgFUS has also been used to disrupt the blood-brain barrier for improved blood delivery and induce neuromodulation (Jonathan and Grissom, 2018).

Besides HIFU, MRT has been optimized for coupling with other heating techniques such as radiofrequency (RF) and microwave (MW) irradiation, and also for use in laser interstitial thermal therapy (LITT) and photodynamic therapy (PDT). Temperature control is especially delicate in situations where only relatively mild hyperthermia is to be applied, i.e., when the goal is not tissue ablation but rather tissue sensitization to other treatment regimens such as radiation or chemotherapy, or enhancement of the immune system. Although many of the most recent developments have been tested in animal experiments only, there also is a sizable number of new applications for which experience with human subjects is available. Although this review focuses on the most recent advances in MRT, it does not cover common pitfalls of PRF methods in general and their circumvention or resolution; this issue has been subject of a recent overview (Winter et al., 2016). MRT work published more than 5–6 years ago will only be mentioned where this is required to provide context for, and better understanding of, more recent work; likewise, reports on clinical routine applications will only be mentioned if they appear to represent new trends that can be expected to further extend the range of medical MRT in the future.

Finally, we will also discuss a very recent MRT technique able to generate multiparametric quantitative information on the statistical distribution of absolute temperature values in a given tissue or hydrogel volume. The novel paradigm underlying this innovative extension of classical PRF methods requires an advanced analysis of the line shape of the water ^{1}H NMR spectroscopic resonance and, in this way, yields statistical temperature profiles not limited by any voxel size (as opposed to chemical shift-based phase imaging). The proof of principle for this particular qhMRS (quantitative heterogeneity MRS) approach has been established recently for *ex vivo* tissue and hydrogel samples. Its potential to afford significant thermal information complementary to that provided by conventional phase image-based PRF methods, which only detect relative temperature changes, will also be discussed.

THE METHODOLOGICAL GROUNDWORK: ADVANCES IN MRS AND MRI TEMPERATURE METHODS

Avoiding Motion Artifacts by Keeping up with Moving Body Tissue: Acceleration of Thermometric Imaging by Phase-Based PRF

The phase-based water PRF method is by far the most popular temperature MRI method, in particular in clinical applications. First proposed by Ishihara et al., this technique is in fact a temperature difference method: a baseline phase map obtained from an object before heating (or cooling) is subtracted from a second phase map obtained during or after temperature change (Ishihara et al., 1995). The difference in phase between any two corresponding pixels of the two maps is directly proportional to the temperature difference before versus after heating (or cooling) for the underlying voxel. Thus, no information on absolute temperature is obtained based on phase-based PRF thermometry; consequently, phase-based PRF "temperature maps" are actually "temperature change maps" or "temperature difference maps." A classical MRI sequence used for obtaining a phase map is shown in Figure 1; an example of phase maps before and after intervention (temperature change), and the resulting temperature change map, is shown in the top row of Figure 2 (second, fourth, and fifth panels, respectively). (The term sequence refers to any series of sequentially or simultaneously applied RF pulses, gradient pulses, and delays for preparation and acquisition of an MRI or MRS signal.) Already Ishihara et al.'s seminal paper, dealing with uniform heating in moving tissue and comprising a number of phantom and *ex vivo* tissue experiments, had reported that with phase-based PRF, the error for temperature change measurement inside a cat's brain was no larger than ± 1°C (Ishihara et al., 1995). Although this technique has enabled fast imaging of temperature differences in a number of hyperthermia regimes, it was not a true real-time method. However, recent developments have brought this objective within close reach. Zhang et al. have integrated a phase-based PRF sequence with a particular fast, dual echo-based MRI protocol (Zhang et al., 2017); see also Table S1. (In MRI and MRS, the term echo refers to an NMR signal resulting from the recuperation and subsequent loss of spin coherence; an echo may be generated by applying an appropriate RF or magnetic-field gradient pulse following initial loss of coherence after excitation.) This approach has been validated

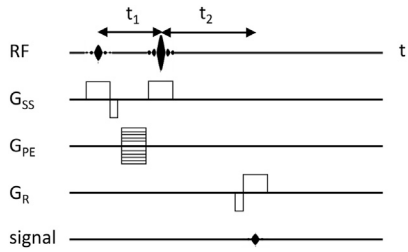

Figure 1. Pulse Sequence for Obtaining Phase Maps Used to Generate Phase-Based PRF Temperature Difference Maps

RF, transmitter radiofrequency pulse; G_{SS}, magnetic-field gradient pulse for slice selection; G_{PE}, magnetic-field gradient pulse for phase encoding; G_R, magnetic-field gradient pulse for readout; signal, echo (receiver input). The difference between delays t_1 and t_2 encodes the difference in chemical shift due to the temperature change as a phase value. This diagram represents the original, most basic sequence used by Ishihara et al. when first introducing MR thermometry by phase-based PRF (Ishihara et al., 1995). Although this sequence includes a spin echo (caused by a 180° RF pulse preceded by a 90° RF pulse), most newer phase-based PRF protocols work with gradient echoes (no 180° RF pulse involved) and may be significantly more complex. In all cases, the phase evolution is a function of the echo time. (For the physical background of phase imaging based on gradient echoes, see, e.g., chapter 11.2.3 of Haacke et al., 1999.) In phase-based PRF thermometry, at least two phase maps are generated based on the water proton resonance. The first phase map is acquired at a reference temperature (typically before heating the object to be studied) and serves as a baseline map. The second (and any further) phase map of the same object is acquired during subsequent temperature change (typically upon heating), under otherwise identical experimental conditions. Subtraction of two phase maps acquired at different temperatures yields an image directly representing phase differences and, with appropriate calibration, temperature differences.

in vitro (use of a temperature phantom) and *ex vivo* (swine kidney). The *in vitro* phantom was designed to generate a stable temperature gradient; the PRF-measured temperature differences were in good agreement with values obtained through fiber optic temperature sensors. The authors anticipated further improvements of this method by porting the calculation of temperature difference maps online (currently performed offline), using a parallel algorithm and a model-based reconstruction technique, in analogy to a similar technique previously developed by the same authors for real-time velocity maps (Untenberger et al., 2016). The ultimate goal is to create an automated protocol that (1) allows for user-selectable spatio-temporal resolution and contrast and (2) can be run without expert knowledge.

Intended or unintended movement of a subject (patient, experimental animal) during image acquisition is a common source of artifacts in MR images. In MRT, breathing is the principal cause of such artifacts. For this reason, MRT images frequently need to be motion corrected; for instance, the authors mentioned above (Untenberger et al., 2016) suggested a method for improved image correction for breathing movements. Motion correction of MRT images, although discussed throughout this review, is not the only way of dealing with artifacts caused by breathing movements; an obvious alternative (or complement) is acquiring images using breath-hold techniques. Bing et al. have investigated the feasibility of circumventing breathing-related motion artifacts by repeated forced breath holds during delivery of MRT-controlled HIFU mild hyperthermia (Bing et al., 2019); see also Table S1. First, stability and uniformity of temperature measurement as a function of anatomic location were determined in patients (children with cancer) without breath hold, by using a phase PRF-based magnetic-field gradient echo, echo planar imaging (EPI) MRT sequence (1.5 T) in the absence of HIFU (Tillander et al., 2016). (EPI is a very fast, albeit somewhat artifact-prone, image acquisition protocol because it is designed to allow acquisition of all data required for an image within one or just a few excitation cycles.) Then, the effects of magnetic-field changes associated with respiratory motion were simulated in a phantom study, by moving an aluminum disk along a sinusoidal trajectory close to the phantom (3.0 T). Breath hold was mimicked by stopping the movement of the disk. Here, HIFU was applied through 1.2-MHz sonications. *In vivo* experiments were performed in ventilated pigs (tumors located at different sites), with or without forced breath hold. The authors determined the accuracy of temperature changes measured by MRT (mean temperature change from baseline), temperature uniformity (spatial standard deviation of temperature within region of interest), and temperature stability (temporal standard deviation within this region of interest) by using a fiber optic probe as a reference. Breath hold appeared to improve temperature control but may still have to be complemented with motion compensation techniques (numerical values obtained for accuracy, uniformity, and stability of MR thermometry are presented in Table S1).

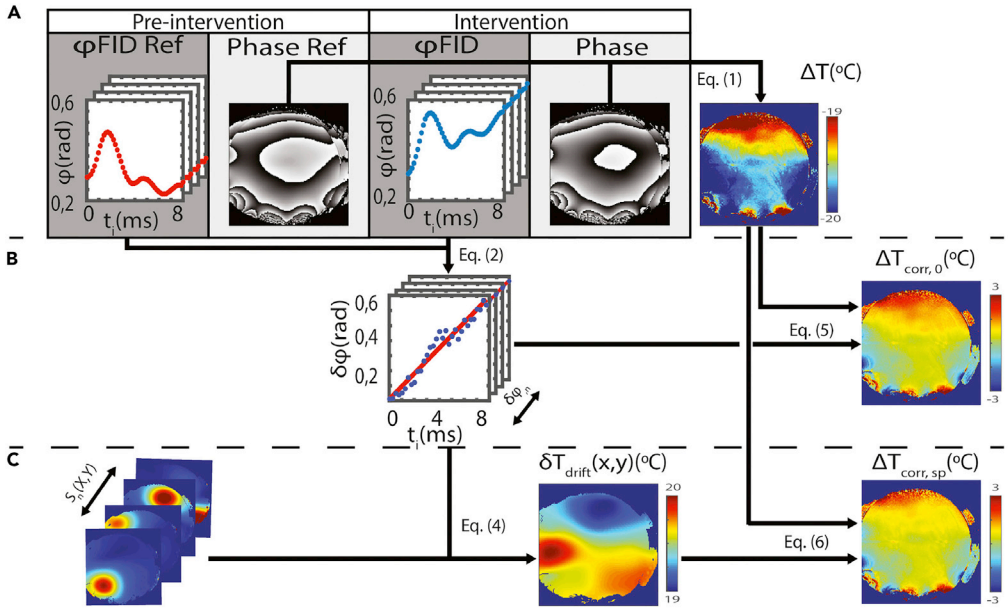

Figure 2. Phase-Based PRF Temperature Difference Mapping Employing Multiple Coil Elements for MRT

Procedure for spatially averaged versus spatially resolved magnetic-field (B_0) drift correction in a phantom experiment.

(A) A spatially nonselective FID was acquired immediately before the associated phase image for each coil element, both at the "pre-intervention" stage (i.e., to provide reference phases, ϕFID Ref, before heating) and at the "intervention" stage (i.e., upon moderate heating, ϕFID). If the PRF map is calculated without B_0 drift correction (i.e., ignoring the FID-based phase information), grossly erroneous temperature differences (ΔT, top right) are obtained due to the B_0 drift occurring between the acquisitions of the two images.

(B) The phase alterations occurring between the pre-intervention and intervention stages are determined from the FIDs for each coil element, n, ($\delta\phi_n$), then spatially averaged over all coil elements and used for B_0-correcting the PRF map representing ΔT (0^{th}-order correction). The resulting temperature differences ($\Delta T_{corr,0}$, center right) are now in the expected range for mild hyperthermia.

(C) Further refinement is obtained by allowing for spatially resolved B_0 drift differences within each 2D image. This is achieved by (1) generating, based on a separate reference scan, 2D coil sensitivity profiles ($S_n(X, Y)$, bottom left) for all n coil elements, and (2) creating a 2D phase correction algorithm based on the FID-derived phase differences, $\delta\phi_n$ (middle center), weighted by said sensitivity profiles. The map resulting from the combination of (1) and (2) represents a spatially resolved frequency drift correction $\delta\omega_{drift}(x, y)$ that may be interpreted as a pseudo-MRT image depicting $\delta T_{drift}(x, y)$ (bottom center). The latter image is then used for (3) B_0 drift correction of the uncorrected phase PRF image (top right) yielding an improved phase PRF MRT image ($\Delta T_{corr,\,sp}$, bottom right). (Designations Equations (2)–(6) refer to the paper cited below.)

Reproduced from Ferrer et al. (2020) with permission obtained through the Copyright Clearance Center.

Seeing Better What Matters in Thermometry: Keep Noise down and Spatial Resolution up in Phase-Based PRF

Fast MRI acquisition schemes used for thermometry frequently suffer from a low signal to noise ratio (SNR), as a consequence of fewer acquired measurements due to under-sampling. Since noisy temperature difference maps may have an impact on therapy control and endpoint detection, filtering methods have been developed for adequate denoising. Zachiu et al. have suggested an adaptive non-local-means filter for real-time MRT (Zachiu et al., 2017). This particular filter with real-time capabilities takes into account not only spatial information but also information available from previous measurements within the same series of phase-based PRFS (PRF shift) temperature maps. The proposed spatiotemporal filter dynamically and automatically adapts filtration strength. This approach improved filtered data especially in the focal point and its surroundings and was tested *in silico*, *ex vivo* (on a calf liver, with 20 W of RF power over 50 s), and *in vivo* (on a porcine kidney, with 250 W of acoustic power over 50 s under anesthesia).

A different approach to improving the SNR consists in optimizing the phase-based PRF sequence used. Ciris et al. have provided an extensive optimization test for two different dual-pathway MRI acquisition

sequences (Ciris et al., 2017; Madore et al., 2011; Yuan et al., 2012) that can be combined with PRF; see also Table S1. (Dual pathway refers to any sequence that allows the acquisition of two images [rather than one], produced by two different signal pathways. Here, two pathways that have maximum temperature sensitivities at different moments in the sequence are employed to improve the overall temperature sensitivity [or "temperature-to-noise ratio," in these authors' particular language] of the MRT sequence.) Their Monte Carlo simulations as well as phantom and *in vivo* validations for many different organs aimed at determining, by way of relaxation time MRI, the conditions under which either dual-pathway sequence is more advantageous, notably as a function of acquisition parameters and tissue type. The newest paper (Ciris et al., 2017) provides information needed to optimally choose either dual-pathway sequence; however, no actual heating experiments demonstrating that the predicted SNR improvements are indeed reflected in increased precision and/or accuracy of temperature difference measurements (when the dual-pathway acquisition sequences are combined with PRF) are presented.

Besides SNR, spatial resolution has been given renewed attention in temperature imaging over the past few years. Jonathan et al. have developed an advanced phase-based PRF approach to achieve optimal spatiotemporal resolution in 3D maps of temperature changes (Jonathan and Grissom, 2018). Their method is very similar to a previously known method originally developed for motion correction (Graedel et al., 2017). The authors compared *in vivo* results of their new technique on healthy volunteers with those of the routinely used 2DFT sequence (Lipsman et al., 2013) and found a somewhat larger temperature uncertainty (0.4°C versus 0.27°C), a small trade-off (value still significantly smaller than 1°C) for being able to cover an entire organ at high spatial resolution (1.5 × 1.5 × 2.75 mm).

Keeping Perturbations of Thermometry at Bay: The Struggle against Effects of Air, Fat, and Drifting Magnetic Fields on Phase-Based PRF

In mild hyperthermia treatment protocols, temperature mapping over extended periods of time is common. Therefore, magnetic-field drifts of the MRI scanner may result in major temperature errors if left uncorrected. Ferrer et al. have suggested a technique for spatially resolved field drift correction (Ferrer et al., 2020); see also Table S1. Phantom heating experiments were conducted by way of 4-min HIFU sonications, alternated with 1-min cooling periods, over a total of 35 min. Without correction for field drift, the temperature error was on the order of 18°C at 1.5 T magnetic field strength and almost 100°C for 3.0 T, when referenced to the values obtained by a fiber optic thermometer probe. The median error was reduced to about 1°C for a 0^{th}-order correction method (average over all coil elements) and somewhat better for a spatially resolved correction method (Figure 2). *In vivo* tests on a healthy volunteer revealed similarly reduced temperature errors.

Chemical shifts of protons from fatty acid chains (e.g., from the methylene protons) do not significantly change with temperature (see also subsection "Beyond Classical Phase-Based PRF and MR Spectroscopy: New Alternative MRI Thermometry in the Presence of Fat"). Therefore, PRF-based thermometry cannot be applied to fatty tissues but has recently been combined with T_1-based thermometry to create temperature maps from body regions that contain both aqueous and adipose tissues (Zhang et al., 2019); see also Table S1. (T_1 is a time constant characterizing the return of nuclear magnetization to equilibrium after perturbation by radiofrequency excitation in a magnetic field.) T_1 varies as a function of molecular structure and physicochemical properties such as temperature and can thus be used as an alternative tool to measure temperature (see also subsections "Beyond Classical Phase-Based PRF and MR Spectroscopy: New Alternative MRI Thermometry in the Presence of Fat"; "Dealing with Misleading Temperature Measurements: Study of Artifacts in MRT"; and "Providing Stability and Safety in Mild Hyperthermia Using Ultrasound: MRT in Particularly Challenging Non-ablative Applications"). Akin to Jonathan et al.'s method (Jonathan and Grissom, 2018), Zhang et al.'s approach was tested by way of ultrasound heating experiments on phantoms and non-heating human subject experiments. In addition, *ex vivo* ablation experiments were performed on porcine muscle/fat samples; here, the temperatures measured by phase-based PRF and T_1 were consistent with optical temperature probe readings, with an absolute mean difference within 2°C.

Besides instrumental (hardware or software-based) PRF developments, MRT improvements have also been achieved by conditioning the object to be analyzed. For instance, there is a major difference in magnetic susceptibility between gases and tissues that may affect the phase of the signal to be measured, in particular in the presence of unpredictable motion of the gas volume, which would result in temperature errors even with motion correction applied. Thus, phase PRFS-based MRT in the pancreas has been enhanced by Ferrer et al. through

filling the digestive tract with an appropriate fluid (here, pineapple juice) to exclude the presence of bowel gas close to the tissue volume to be studied (Ferrer et al., 2018). The authors have experimentally shown that, with respiratory gating and motion compensation, but without bowel filling, the standard deviation may amount to about 10°C in the pancreas head, which would lead to problems in treatment evaluation and safety monitoring during thermal therapy. Filling the bowel through oral intake of 500 mL fluid increased the precision to 2°C. (Pineapple juice was chosen because of its high manganese content leading to short relaxation times, as had been demonstrated previously [Arthurs et al., 2014].)

Making Temperature Measurement Absolute: The MR Spectroscopic Alternative to Phase-Based PRF

Although most recent MRT research was focused on the PRF technique based on indirect detection of chemical-shift changes of the water proton signal via phase changes (see the previous three subsections), direct measurement of the water proton chemical shift through single-voxel MRS and CSI (aka MRSI, MR spectroscopic imaging) has also been applied and further developed over the past years. (Note that, in the MRT literature, the abbreviations PRF and PRFS are sometimes used to specifically denote phase detection PRF methods. In this review, PRF and PRFS are used as to include both PRF-based approaches, i.e., phase detection PRF [as discussed in the preceding subsections] as well as spectroscopic PRF [as discussed in this subsection].) One of the most important reasons for the continued use of the spectroscopic PRF approach has been its potential to easily obtain values for absolute temperatures rather than relative temperature changes over time. This is because reference signals with temperature-independent chemical shifts can usually be obtained in the same ^{1}H MRS experiment from suitable metabolites present in the tissue of interest (methyl resonances of choline [cho], creatine [Cr] or *N*-acetylaspartate [NAA], and methylene resonances from mobile lipids; see subsection "Double-Checking Temperature Measurements: Calibration and Confounding Factors in MRT" for calibration issues). For instance, Mintzopoulos et al. have used sequentially acquired water-suppressed and unsuppressed point-resolved spectroscopy (PRESS) images in different regions of the monkey brain to detect temperature changes after infection with simian immunodeficiency virus (SIV) that is closely related to the human immunodeficiency virus (HIV) (Mintzopoulos et al., 2019). Here, the chemical-shift difference between the methyl resonance of NAA and the water proton resonance was used to calculate absolute temperature for each voxel. Two weeks after SIV infection, the authors found a transient temperature increase by < 1°C in different brain regions; this effect was particularly significant for the frontal and parietal cortex regions measured. The temperature increases were positively correlated with the tissue total cho content (comprising choline, phosphocholine and glycerophosphocholine) that was also determined by ^{1}H MRS (correlation significant for the frontal and parietal cortex). This study also underlines an added advantage of measuring tissue temperature by MRS instead of phase maps, namely, the simultaneous measurement of metabolite levels.

MR measurement of temperature differences as small as those mentioned in the preceding paragraph (variations by < 1°C across a given volume of interest) is sensitive to confounding parameters that are not of critical importance in more common hyperthermia-related measurements (heating by > 3°C; for ablation by >>3°C). Such a confounding parameter is the difference in magnetic susceptibility between different tissues. Maudsley et al. have refined MRSI thermometry by taking into account magnetic susceptibility variations within the human brain, thus increasing the precision of temperature maps covering the entire human brain volume (Maudsley et al., 2017); see also Table S1. The authors applied their method to an MRSI database originally acquired for a total of 150 normal subjects in order to study brain metabolism. Here, the relative contributions of white matter (WM) and gray matter (GM) to each MRSI voxel were calculated with the help of MR images weighted by the longitudinal water proton relaxation time, T_1. Using this information, the authors obtained a best-case reproducibility of $\pm$0.2°C through a complex procedure briefly outlined in Table S1. However, they also noted that the accuracy of their temperature measurement remained unverified because, as in all MRS studies of brain temperature, chemical shift-versus-temperature calibration factors cannot be determined separately for GM and WM using *in vivo* techniques. Notwithstanding, this tissue-specific refinement of temperature measurement appears to be valuable in analyzing small temperature differences within the human brain and may be implemented in other advanced MRSI-based thermometry protocols to be discussed below (Lutz and Bernard, 2017, 2018a). However, any translation to other heterogeneous tissues will be very limited, as adequate definition of microscopic tissue heterogeneity through *in vivo* MR methods is not usually accessible in other organs or in tumors. Two general drawbacks of MRS-based compared with phase-based PRF temperature mapping are the reduced spatial resolution and the difficulty of sampling large volumes. In addition, the accuracy of temperature measurement

is limited by the temperature-independent linewidth of the water resonance in relation to temperature-dependent chemical-shift variations of that resonance, although the effects of the former can be compensated for in some instances as pointed out in comments on (Lutz and Bernard, 2017, 2018a) in Table S1.

The water proton resonance is not the only MRS peak usable for PRF-based thermometry. In principle, any temperature-dependent chemical-shift variation between two signals of an MRS spectrum can be used for MRT. Wermter et al. have measured the temperature dependence of chemical-shift differences between resonances of 11 brain metabolites (Wermter et al., 2017); see also Table S1. However, the (linear) temperature dependence of these metabolite peaks was about one order of magnitude smaller than that of the water ^{1}H resonance (<0.001 ppm/°C) (Lutz et al., 1993). Therefore, it is unlikely that ^{1}H MRS peaks other than that of water will be used as an *in vivo* "thermometer," except in cases where (1) spectra with unsuppressed water resonances are unavailable, and (2) very large temperature effects are to be analyzed, e.g., in tissue ablation by HIFU.

Revealing the Finer Details of Thermal Heterogeneity: Decryption of the Statistics Encoded in Thermometric MR Spectra

All methods discussed in the four preceding subsections and the following seven subsections have in common that they determine one temperature value (or one temperature difference value) per volume or voxel measured. As a result, any temperature map generated with a phase-based or a spectroscopic MRT technique will only convey one temperature value for each image pixel. Consequently, although these maps are able to reveal temperature gradients between voxels, they cannot detect or even quantify intra-voxel temperature gradients. However, in hyperthermia treatment and cryotherapy, significant temperature gradients may occur not only between but also within selected tissue volumes or voxels. In other words, such a volume or voxel is likely to be characterized by a finite distribution of temperature values within a particular temperature range.

Very recently, a new paradigm for spectroscopic evaluation of the water ^{1}H resonance line shape has been suggested, aimed at overcoming these limitations (Lutz and Bernard, 2017, 2018a); see also Table S1. This new method is based on the fact that, in the presence of thermal heterogeneity (i.e., temperature gradients) within a given volume, the broad water ^{1}H resonance representing that volume is in fact composed of overlapping individual lines with varying chemical shifts, the latter being defined by the local temperatures at the nuclei detected. However, the resulting envelope line shapes are not simply broadened but actually encode quantitative information on the statistical distribution of temperature values within the thermally heterogeneous volume. The authors suggested to decode this information by statistical line shape analysis, thus integrating established NMR line shape analysis and statistical curve shape analysis (Lutz and Bernard, 2017). This analysis results in at least eight statistical parameters, aka "descriptors," that quantitatively describe the statistical distribution of temperature values within the measured volume or voxel (for details of descriptors see Table S1). In other words, the classical spectroscopic MRT measurement only extracts one average value from each single volume or voxel-based MR spectrum as stated above, whereas the new approach exploits the entire water proton MRS line shape encoding the total distribution of temperature values existing within the volume/voxel in question. As this new technique allows one to quantitatively analyze thermal heterogeneity, it is termed quantitative heterogeneity MRT (qhMRT), a particular variant from the group of qhMRS (quantitative heterogeneity MRS) methods (Lutz et al., 2013; Lutz and Bernard, 2019a, 2019b, 2018a, 2018b, 2018c, 2017).

This new technique has been validated by computer simulations *in silico*, by gel sample studies *in vitro*, and by investigations of muscle tissue *ex vivo*. Thanks to the strong NMR signal of water protons occurring in the 10^{1}–10^{2} molar concentration range, fast spectra were obtainable from specially designed agarose hydrogel samples exhibiting temperature gradients of approximately 50°C within the phantom at the start of each measurement series (Lutz and Bernard, 2018a). This permitted the acquisition of complete temperature profiles at sub-second temporal resolution during the subsequent thermal equilibration, with at least one profile every 400 ms. The statistical descriptors obtained from each temperature profile give unprecedented quantitative access to the statistical temperature distribution of the samples in question (see Table S1 for the temperature sensitivity of this method). An overview of the entire thermal process as a function of time can be obtained by visualizing the temperature profiles in a 3D presentation (Figure 3) facilitating the detection of critical changes during thermal equilibration, whereas the time course of the calculated descriptors provides quantitative time-dependent data on statistical temperature distribution (Figure 4). Like other qhMRS applications, qhMRT can be integrated with MRSI and thus generate maps presenting the spatial organization of tissue or hydrogel areas with different statistical descriptors of

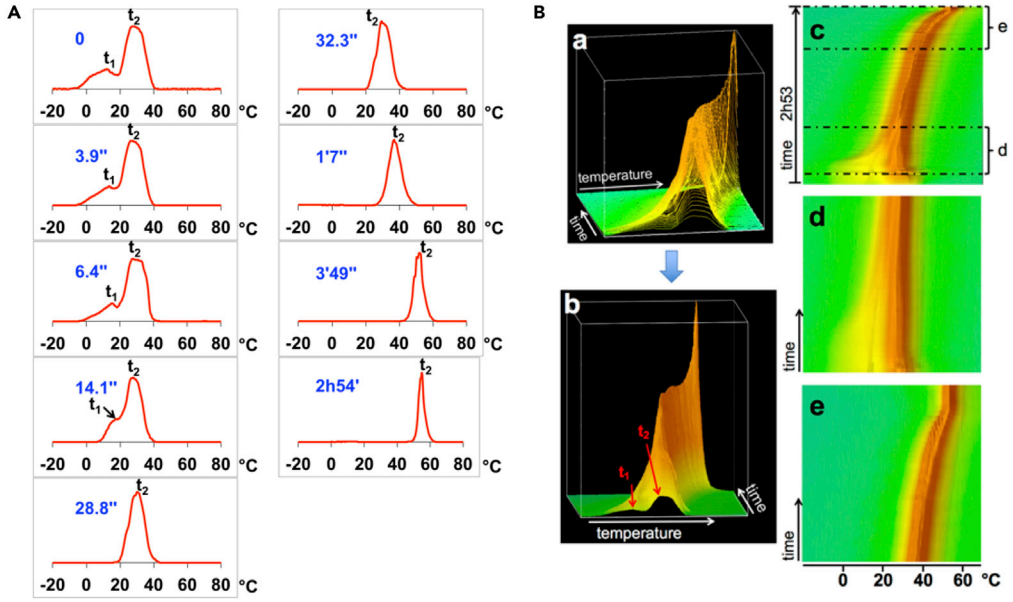

Figure 3. Experimental Validation of qhMRT

Graphic presentation of temperature profiles derived from an experiment for monitoring the evolution of heat exchange in a thermally heterogeneous gel sample surrounded by an air stream at a constant temperature (see Table S1). Temperature gradients within the sample were largest at the start of the experiment (after placing a narrow tube filled with cold gel into a wider tube filled with hot gel). Toward the end of the experiment, thermal equilibrium was reached throughout the combined sample, at the temperature of the air stream.

(A) Selected height-normalized temperature profiles for different time points after the first measurement. The first temperature profile, derived from a spectrum that had been acquired when heat exchange between the tubes had only begun to evolve, clearly shows two partially resolved peaks; the origin of the lower (higher) peak was the narrow (wide) tube. As heat exchange progressed, the two peaks coalesced progressively and became very narrow after several minutes. The final temperature of the gel in both tubes was defined by the temperature of the hot air stream around the outer tube (about 55°C, as indicated by the peak derived from the spectrum measured about 3 h after the first acquisition).

(B) 3D rendering of stacked plot of all temperature profiles after area-normalization. (a) Oblique view of profiles. (b) Oblique view of profiles presented as a surface plot to facilitate inspection of the overall evolution of temperature profiles over time. (c) View of the entire 3D surface plot from top. (d) and (e) View of portions of (c) to facilitate inspection of finer details at the start (d) and the end (e) of the experiment.

Reproduced from Lutz and Bernard (2018a), no permission required.

temperature distribution (Lutz and Bernard, 2018a). If successfully translated to practical applications, this approach would add novel, detailed information on thermal behavior in the context of thermotherapy and other clinical applications, and in the production and use of hydrogel biomaterials.

Beyond Classical Phase-Based PRF and MR Spectroscopy: New Alternative MRI Thermometry in the Presence of Fat

Since the chemical shifts of fat protons are virtually temperature independent, PRF techniques cannot be used to measure temperature in fat. Therefore, alternative MRI methods have been proposed, based on T_1 or T_2 of the most easily detected fat protons (-CH_2 of the aliphatic chain, in the vicinity of other saturated carbon bonds). (T_2 or transverse relaxation time is a time constant characterizing the spontaneous loss of coherence of nuclear magnetization in a homogeneous magnetic field after perturbation by radiofrequency excitation.) Since the speed of T_1-based methods is limited by SNR, especially at higher magnetic fields where T_1 is particularly long, recent developments focused on T_2-based thermometry methods. Parmala et al. optimized a T_2-based thermometry protocol on four different imagers of different field strengths (1.5 and 3.0 T), using subcutaneous fat obtained from patients in phantom studies, with an optical temperature probe as a reference (Parmala et al., 2016); see also Table S1. This (absolute-temperature) method was tested *in vivo* in a patient undergoing HIFU treatment (Figure 5).

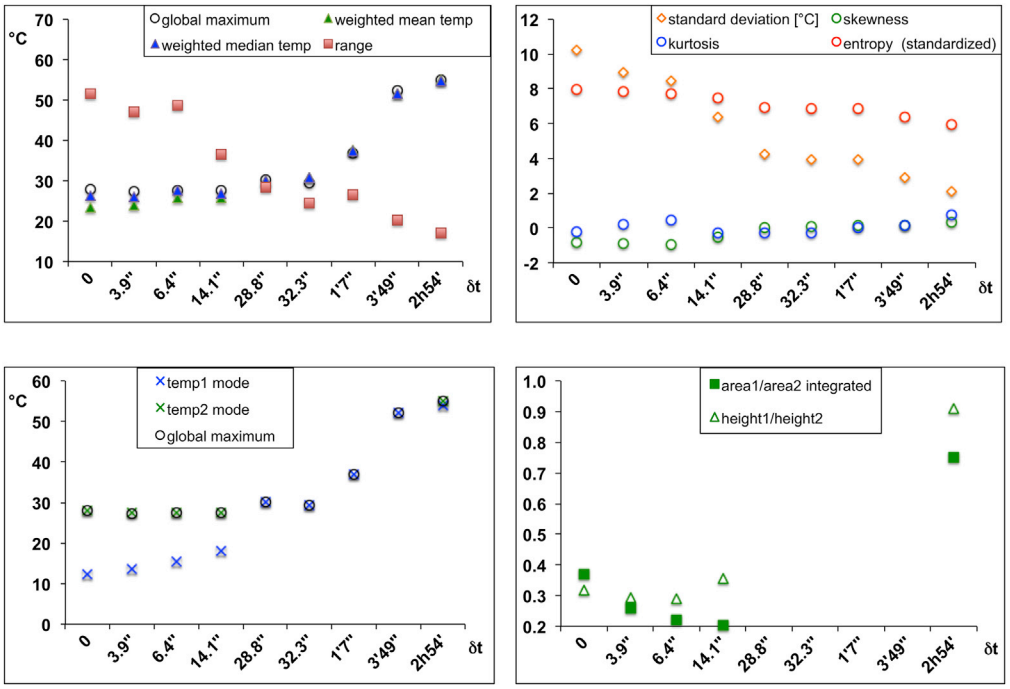

Figure 4. Experimental Validation of qhMRT

Statistical descriptors of temperature distributions as a function of time, derived from temperature profiles shown in Figure 3A (see also Table S1). Weighted mean and median temperatures remain rather stable as long as heat exchange between the two gel compartments dominates thermal behavior (i.e., during the first 30 s); then, means and medians increase to the final value (top left). This is confirmed by the coalescence of the two modes (peak maxima) and their approaching the final temperature (bottom left). Progressive narrowing of the temperature profiles is reflected by decreasing range and standard deviation values (top left and right). Among other descriptors, kurtosis (peakedness), skewness (symmetry), and entropy (evenness, smoothness) offer quantitative measures of the shapes of temperature distribution curves (top right). Two partially separate areas can be distinguished below some of the temperature distribution profiles shown in Figure 3A; for each of these profiles, two separate areas (area1 and area2) below the curve can be quantified, and the temporal evolution of the area1/area2 ratio can be followed as a function of time (bottom right). This also applies to the heights of the individual peaks over these areas (height1 and height2).
Reproduced from Lutz and Bernard (2018a), no permission required.

Although the chemical shifts of fat protons cannot be used per se to measure temperature by PRFS, they may nevertheless play a role in water proton PRFS thermometry, through determination of the water-fat proton chemical shift difference. In fact, in tissues that contain modest quantities of fat, the large temperature-independent methylene lipid resonance at 1.29 ppm can be used as a reference peak for MR spectroscopic (or MRSI) temperature measurement by water proton PRFS, akin to the role of the cho and NAA methyl proton peaks brought into play above in subsection "Seeing Better What Matters in Thermometry: Keep Noise down and Spatial Resolution up in Phase-Based PRF" (Zhu et al., 2017), or of the total Cr methyl proton peak.

It should be mentioned in this context that, in the phase mapping thermometry method, fat peaks may indeed interfere with relative temperature measurement if a significant amount of fat is present in the tissue studied. This is because in the most common forms of the phase mapping method, the MR signal from the entire spectrum is used for phase measurement, not only the water proton signal. However, selective "fat suppression" techniques have been introduced long ago to suppress MR signals occurring at and near the lipid methylene resonance frequency at 1.29 ppm, since this resonance represents the strongest fat peak (Kuroda et al., 1997). To the best of our knowledge, this chemical shift selective phase mapping (CSSPM) method has not been refined in the intervening years to include, for instance, suppression of other fat resonances and major metabolite peaks.

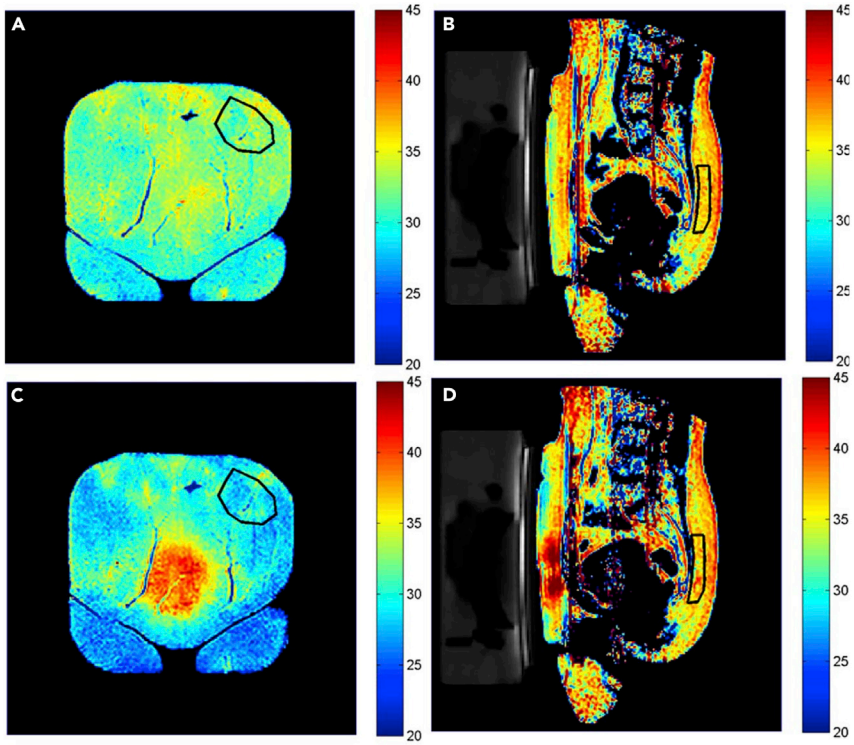

Figure 5. MRT Based on the Temperature Dependence of T_2: *In Vivo* Thermometry in Human Fat

(A) and (B) Temperature maps of a patient before HIFU treatment; (C) and (D) temperature maps of the same patient after a series of 13 HIFU sonications. (A) and (C) Coronal images near the interface between subcutaneous fat and the HIFU table; (B) and (D) sagittal images with view through the HIFU-treated uterine fibroid. The red areas in (C), center, and in (D), next to the HIFU transducer on the left, demonstrate a temperature increase up to about 40°C in the fat region close to the treated fibroid, whereas the fat regions not in the path of the HIFU beam appear blue due to a temperature decrease down to about 25°C caused by the HIFU table actively cooled to 20°C. The temperature of the posterior subcutaneous fat, distant from HIFU table and beam path, remained largely constant, as evidenced by the color coding within the areas outlined by black lines in (B) and (D). The HIFU-targeted fibroid tissue appears largely as a black void in (B) and (D). In this application, fat thermometry serves the purpose of monitoring hyperthermia side effects on non-targeted tissue in real time.

Reproduced from Parmala et al. (2016) with permission obtained through the Copyright Clearance Center.

Instead of suppressing fat resonances, Liu et al. have recently proposed referencing MRI with a stepwise water saturation shift method to obtain accurate temperature difference maps in the presence of fat (Liu et al., 2014); see also Table S1. The authors have demonstrated the feasibility of this method by numerical simulations, phantom experiments (agarose gel with or without cheese), and an *in vivo* animal experiment (hyperthermia of mouse legs), with an additional fat suppression pulse. Direct comparison with the phase-based PRF method showed a greatly decreased sensitivity to errors introduced by fat protons. The authors anticipated further increase in speed (the current temporal resolution being limited to 2 min) by implementing faster imaging sequences. The resulting voxel size is sufficiently large to "hide" intra-voxel thermal heterogeneity, notably due to unresolved temperature gradients along the long axis of the voxels (issue addressed in more detail in the previous subsection). An additional approach to *in vivo* MRT in the presence of fat, albeit based on a different physical principle, is presented separately in subsection "Choosing a Special Method for a Special Situation: Temperature Measurement through Intermolecular Coherences in Bone Marrow and Particular Adipose Tissues".

Kim et al. have combined fat-referenced PRFS (FRPRFS) with MR elastography (MRE) to monitor thermal ablations by HIFU (Kim et al., 2020); see also Table S1. MRE provides information on the tissue ablation process that is complementary to information provided by thermal maps and had previously been applied in the context of hyperthermia, but only in conjunction with classical phase-based PRFS as a temperature mapping technique. Since the latter PRFS approach becomes inaccurate in the presence of fat, the authors

replaced it with the previously developed FRPRFS method that is also phase-based (IDEAL [Hofstetter et al., 2012]). The new approach was tested in a phantom; subsequently, porcine rib muscle samples were tested *ex vivo*, enclosed in a gelatin/milk cream gel. Time-dependent profiles of elasticity (relative stiffness changes, RSC) and temperature changes, derived from elasticity maps and temperature maps, respectively, validated the feasibility of the suggested FRPRFS/MRE method.

Boosting Temperature Effects on Chemical Shift: Focus on Protons in Paramagnetic Lanthanide Complexes

Although the temperature dependence of the chemical shift is significantly more pronounced for water protons than for protons of virtually all other naturally occurring compounds in biological tissues, resonances from certain lanthanide complexes can be far more temperature sensitive than those from water. This is because unpaired electrons, present in paramagnetic ions such as lanthanide ions, have a dramatically increased magnetic moment when compared with (diamagnetic) protons. Under appropriate circumstances, this effect results in paramagnetically shifted resonances for nuclei close to the paramagnetic ion. This has long lead to the suggestion to use the protons of lanthanide chelates for temperature measurement (Aime et al., 1996). Among these, macrocyclic complexes of thulium possess protons with particularly temperature-dependent chemical shifts, e.g., Tm-DOTP^{5-} (0.93 ppm/°C for the H6 proton). The finding that the chemical shifts of several different protons of this complex vary not only with temperature but also with pH has been used to measure temperature maps and pH maps simultaneously, in phantoms and *in vivo* (rat brain) (Coman et al., 2009).

Although the Tm-DOTP^{5-} method directly determines chemical shifts based on CSI acquisitions, an alternative approach relies on indirect chemical-shift measurement by paramagnetic chemical exchange saturation transfer (paramagnetic CEST or PARACEST) imaging (McVicar et al., 2013). In this case, temperature maps are obtained using the chemical shift of the CEST peak of a Tm^{3+} complex with a DOTAM-glycine-lysine ligand (DOTAM = 1,4,7,10-tetrakis(carbamoylmethyl)-1,4,7,10-tetraazacyclododecane). pH maps are obtained simultaneously using the amide protons (pH determined from the temperature-independent line width of the asymmetry curve of the CEST spectrum). Regardless, newer developments in this direction have been extremely scarce during the past years, most likely because continuous improvements of *in vivo* MRT methods that do not require injection of reporter molecules such as lanthanide chelates into the body have rendered lanthanide-based techniques unattractive.

A notable exception is the special case of thermometry of flowing blood (Heyn et al., 2017). Since the practical application envisaged was mild hypothermia, very high temperature sensitivity was required. Therefore, the authors have developed a thermometry method based on proton resonances from thulium chelates, characterized by a temperature sensitivity of 0.6 ppm/°C for the methyl protons of TmDOTMA. The chemical shift of these protons is insensitive to pH variations, as opposed to that of the TmDOTP^{5-} H6 protons mentioned above. Separate PRF phase images were obtained selectively for these methyl protons and for water protons, to obtain absolute temperature values. This method was validated by phantom and animal experiments (vena cava and aorta in mouse abdomen). The accuracy of absolute temperature values measured *in vitro* was within the error of the fiber optic thermometer used for ground truth measurements ($\pm$0.5°C). Of course, a disadvantage of all chelated lanthanide agents is that their *in vivo* use is basically limited to animal experiments because legal approval for human use is unavailable at present, although the toxicity of these compounds is believed to be in the range of that of classical, approved MRI contrast agents (Heyn et al., 2017).

Choosing a Special Method for a Special Situation: Temperature Measurement through Intermolecular Coherences in Bone Marrow and Particular Adipose Tissues

A rather original approach to temperature MRI had originally been suggested a decade ago by W.S. Warren's group (Galiana et al., 2008; Jenista et al., 2010); see also Table S1. Their intermolecular zero quantum coherence (iZQC) technique is based on flipping up a water proton spin while flipping down a lipid (fat) proton. This procedure detects absolute temperature based on the frequency difference between the two spins. However, (1) it only works in tissues where fat and water protons coexist roughly at a distance of $\approx$100 μm (e.g., in particular adipose tissues, red bone marrow [RBM] [Davis and Warren, 2015]), and (2) effects of any magnetic-field inhomogeneity occurring on a smaller scale than that distance hamper temperature measurement. Moreover, as in all image-based thermal analysis methods, temperature gradients occurring on a scale smaller than voxel size (with each voxel being represented by one pixel in the

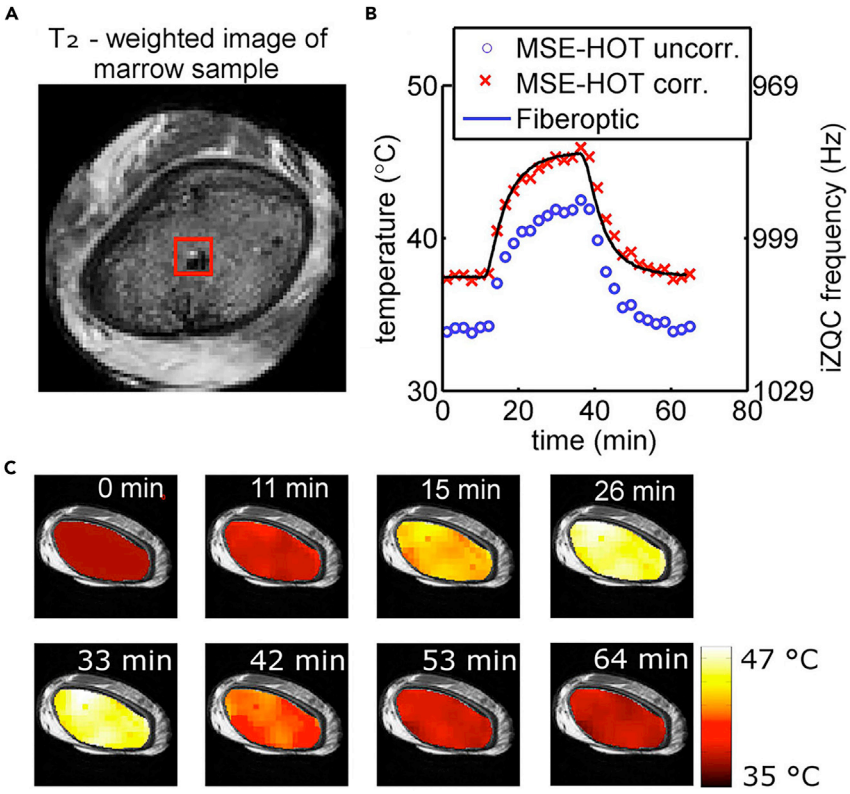

Figure 6. Temperature Mapping by iZQC Thermometry in Tissue Containing Both Water and Fat; Proof of Principle for *Ex Vivo* RBM Samples

Temperature measurement by the MSE-HOT sequence (see Table S1) was validated by comparison with results from a fiber optic thermal probe.

(A) A morphological T_2-weighted image of a porcine rib sample shows the location of the fiber optic probe within the RBM (dark region in the bottom right corner of the region of interest used for analysis, outlined as a red square).

(B) The temperature change over > 1 h during mock hyperthermia (sample heating followed by cooling) is presented for uncorrected MSE-HOT results (blue circles) and for MSE-HOT results corrected by offsetting all temperatures such that the first data point falls on the corresponding fiber optic probe-measured temperature (red 'x' markers). The latter time course corresponded very well with that measured simultaneously with the fiber optic probe itself (black line). Although the temperature coefficients for different RBM samples (and even emulsions used for calibration) are nearly identical (3 Hz/°C), the discrepancy between the very high reproducibility and the much lower accuracy was hypothesized to be due to particular differences between microstructures of different RBM samples (and emulsions). These variations may cause different susceptibility effects leading to different absolute temperature measurements in different samples.

(C) Temperature maps overlaid on T_2-weighted images during the same heating and cooling process. These maps provided the data for preparing the diagram shown in (B).

Reproduced from Davis et al. (2016) with permission obtained through the Copyright Clearance Center.

temperature map) would not be detectable. In addition, almost all applications of inhomogeneous zero or multiple QC in biological systems are limited by the SNR of the QC signal (Davis et al., 2016).

More recently, the SNR of the iZQC thermometry method was improved by Davis et al. (2016). This was achieved by replacing the original single spin echo (SSE) version of iZQC thermometry by a multiple spin echo (MSE) version. The increased SNR resulted in a greatly decreased standard deviation of temperature, due to echo averaging and suppression of J coupling of the fat methylene protons (see Table S1). When compared with the temperature measured by an optical fiber system, this translated to an accuracy that improved from an absolute uncertainty of 2.0°C to 1.7°C (= root-mean-square deviations or "RMSD errors"). The corresponding relative uncertainty for temperature change decreased from 0.8°C to 0.6°C. Based on experimental evidence, the authors ascribed the relatively large difference between absolute and relative uncertainty to variations in the microscopic structure of samples such as RBM (Figure 6) because the temperature coefficients were nearly identical (3 Hz/°C). For instance, variations in the

presence of nonspherical adipocytes or lipid droplets that shift the fat methylene resonance frequency may cause alterations in susceptibility heterogeneity in conjunction with the susceptibility difference between aqueous and lipidic microenvironments.

Integrating Dedicated Tools for Clinical Hyperthermia: Combination of MRT with Novel RF, MW, or US Applicators

Carefully controlled deposition of thermal energy to hyperthermia targets, and protection of adjacent tissue from overheating, is mandatory for all hyperthermia methods. Therefore, manufacturers of hyperthermia equipment (including applicators) provide dedicated software for treatment planning. However, direct temperature measurement in treated tissues has revealed that the temperatures actually achieved in tissue may deviate by more than 2°C from calculated values, which is considered to be clinically unacceptable (Aklan et al., 2019). To a large extent, this discrepancy is due to tissue heterogeneity with respect to blood perfusion and liquid content, notably in tumors such as soft-tissue sarcoma (Aklan et al., 2019). This underlines the urgent need for real-time temperature control during hyperthermia treatment, which is only feasible if the device serving as the source of energy is fully compatible with the thermometry device.

Invasive thermometry using multiple RF-compatible Bowman thermistors inserted into the tips of catheters has been studied in the context of hyperthermia by RF but was poorly tolerated by patients, resulting in low patient numbers (Aklan et al., 2019). Another disadvantage of thermistors is low spatial resolution; in fact, stepwise displacement of the thermistor (within each of the few catheters that can be placed in the tissue to be treated) is the only way to obtain information on spatial temperature distribution.

As a consequence, further development, optimization, and evaluation of MR-compatible energy sources for hyperthermia applications has been undertaken in the past years. Interstitial hyperthermia (based on RF/MW) is very invasive, whereas ultrasound-based techniques are minimally invasive and inherently safer (Adams et al., 2016). Thus, owing to the dominating role of ultrasound as energy source in hyperthermia, the performance of new MR-compatible ultrasound applicators has been tested in the past years. Adams et al. have designed two alternative ultrasound applicators for MR-guided thermal ablation of pancreatic tumors (one with planar and one with curvilinear transducer geometry) and have evaluated these in a porcine model (Adams et al., 2016). Taking into account the proximity of the pancreas to the stomach and the duodenum, they fabricated applicators by integrating a directional ultrasound transducer array with an endoluminal catheter, the latter to be introduced either into the stomach (for the porcine model) or into the duodenum (for future human applications, by reason of anatomical differences between the porcine and human intestinal tract and pancreas; Figure 7, top). The two applicators were tested *ex vivo* (porcine cadaver) and *in vivo* (pig). For active MR tracking, spiral tracking coils were integrated on the backsides of the transducer assembly fixtures. Thermometry was performed with a phase PRF-based gradient echo (GRE) sequence, controlled by a software environment allowing interventional applicator tracking and imaging. This enabled multislice temperature monitoring at an update time of about 3 s per slice (Figure 7, bottom). The results of this preliminary feasibility study demonstrated that MR-guided endoluminal ultrasound applicators can generate volumetric thermal ablation in pancreatic tissues from within the GI tract. MR guidance provided effective localization and positioning of the applicator, as well as the potential for monitoring volumetric temperature elevation. One weakness of the tested thermometry sequence is the relatively poor temporal resolution achievable. However, further technical refinements as well as preclinical and clinical tests seem to be warranted.

Inducing and Monitoring Changes in Brain Temperature from the outside: Transcranial HIFU Applicators and MRT

Progress has also been made in the development of transcranial MRT applicators. As opposed to the work discussed in the preceding paragraph, Lechner-Greite et al. studied the performance of their ultrasound applicators under conditions of EPI-based phase PRFS, a very fast sequence (Lechner-Greite et al., 2016); see also Table S1. An important issue with all EPI-based imaging is its sensitivity to eddy currents. The latter easily cause imaging artifacts and, therefore, inaccuracies in temperature difference maps, especially in the presence of conductive copper layers in the ground planes of ultrasound transducers. For this reason, the authors redesigned the ground plane of their large phased-array ultrasound applicator and tested a variety of alternative designs. The ground plane was segmented into a variety of alternative patterns. In the particular test chosen by the authors, a star-like segmentation pattern of the ground plane showed the best overall performance in terms of (1) mitigating (local) eddy current-induced geometric

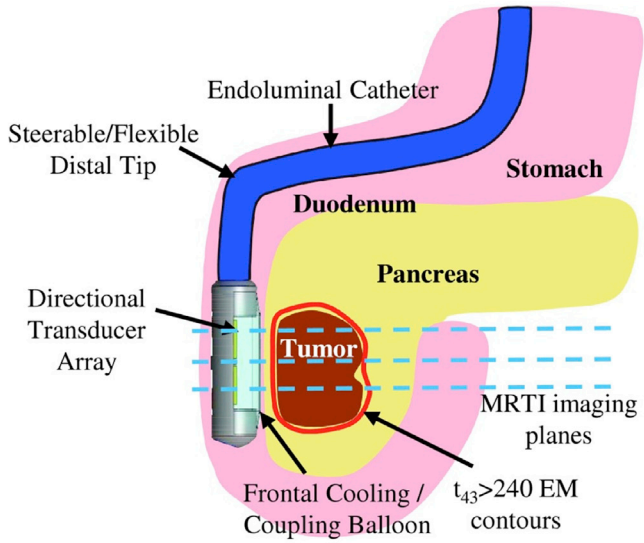

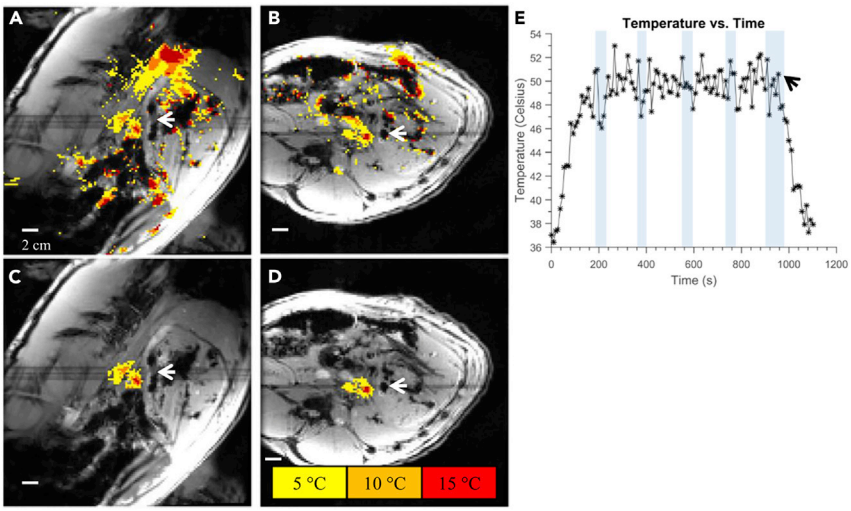

Figure 7. Use of Endoluminal Ultrasound Applicators in Phase PRF MRT-Guided Hyperthermia of Pancreas Tumors: *In Vivo* Pig Model

Top: applicator position in the GI tract (here, in the duodenum for sonication of tumors in the head of the pancreas). Transducer arrays of the dual-planar applicator are configured for lightly focused or diffuse patterns to provide a high degree of spatial control and volumetric heating.

Bottom: (A) sagittal and (B) axial temperature monitoring planes after 6 min of HIFU heating at about 5.5 W/cm^2 applied to each of the two transducers (dark spots next to the tips of the white arrows). Temperature increases during sonication are color-encoded as indicated in the legend. (C) and (D) are identical to (A) and (B), respectively, except that spatial masks were applied to isolate sonication-induced temperature changes versus the motion artifacts clearly visible as spurious color spots in (A) and (B). Sonication resulted in a maximum temperature increase by roughly 20°C. The time course of temperature (E) for a small (3 × 3 pixels) region of interest within the heated region illustrates prolonged temperature elevation of the targeted tissue to about 50°C, with a baseline body temperature of 37°C (black arrow: end of sonication). Temperature measurements during breath-holds are indicated by shaded vertical bars. In order to reduce motion artifacts, multiple baseline phase PRF images were also acquired.

Reproduced from Adams et al. (2016) with permission obtained through the Copyright Clearance Center.

distortions due to fast-switching gradients, and (2) producing accurate MRT maps. However, since distortions greatly depend on the geometry and orientation of the transducer relative to the pulsed gradient coils and the imaging plane, the results of this study should only be considered as a useful starting point for tests under different experimental conditions.

Another approach specifically developed for transcranial HIFU consisted in combining the monitoring of temperature with that of displacement induced by the acoustic radiation force of focused ultrasound sonications at 850 MHz. Ozenne et al. have established an MRI sequence based on classical MRgHIFU and MR-ARFI (MR acoustic radiation force imaging) (Ozenne et al., 2020). The latter technique works through mechanical force rather than heat and has originally been proposed to identify the focal point location in an ultrasound therapy approach known as transcranial ultrasonic stimulation (TUS). TUS has been suggested for transient neuromodulation in epilepsy, Parkinson's disease, chronic pain, and psychiatric disorders. The purpose of Ozenne et al.'s combined method (MR-ARFI-THERMO) is to detect unintended (or intended) thermal effects of TUS while monitoring mechanical displacement. The method was tested at 3 T using a 4-element MR receive coil, with a single-element acoustic phase array transducer. *In vivo* results were obtained from the brain of an adult non-human primate (NHP, here: macaque), following simulation to calibrate the transducer and FUS propagation in the NHP's head. The authors have demonstrated *in vivo* that simultaneous transcranial measurement of thermal rise and displacement is feasible in the brain with FUS. The single-shot gradient echo 2D EPI acquisitions produced displacement and temperature difference maps overlaid on an anatomical MP-RAGE image and allowed for 2-mm isotropic resolution. Using their protocol, the MR-ARFI-THERMO sequence revealed no substantial heating at the FUS focus within the temperature uncertainty of the method (ca. 1°C). Moderate temperature increase (up to 1°C–2°C) was only detected near the skull. Thus, the method was judged to be applicable to (1) improving focusing of the FUS before treatment; (2) differentiating mechanical and thermal effects during US neurostimulation; and (3) preparing a potential second sonication pulse for ablation.

Meeting the Needs of Animal Experiments, and Other Special Requirements of MRT: New Probes, New Coils, and Unusual Applicators in Hyperthermia

Most MR hyperthermia studies on small experimental animals have been conducted on clinical instruments (1.5 or 3.0 T), but for higher spatial and temporal resolution magnetic fields up to 14 T have been used recently. This is a particular challenge for MW-based hyperthermia where the bore size of the magnet is close to the wavelength used for heating (both are in the centimeter range, for typical heating RF of 2.45 GHz). Hence, particular MW applicators had to be developed and tested for this case (Curto et al., 2018). In this work, Curto et al. presented the design and the implementation of such an MRI-compatible hyperthermia system, including a coaxial-type MW applicator with a bandpass filter employed to attenuate spurious frequencies at the MRI proton resonance frequency of 600 MHz (14-T magnet), thereby mitigating electrical interference between applicator and the (micro) receiver coils needed for mouse imaging. The design was guided by a computational model and tested using a tissue-mimicking agar phantom as well as a subcutaneous mouse tumor model. MRT was performed using phase PRFS with a particularly fast MRI protocol (fast low-angle shot, FLASH) and verified for the agar gel phantom by way of fiber optic probes. As a result, despite its small size, the newly developed MW applicator was able to provide heating as required for hyperthermia applications in animals, the latter being studied in the small bore of typical high-field MR magnets.

Although a number of RF applicators are in use in mild-hyperthermia treatment, systematic quality assurance studies are rare. Mulder et al. presented, for the first time, an evaluation of the focal shape, focus position, and volume, as well as off-target heating for a particular MR-compatible RF applicator by using high-resolution 3D MRT (Mulder et al., 2018); see also Table S1. This method represents a far more detailed and accurate measurement than would be possible with the conventional intraluminal temperature probes, as the latter are not inserted into the actual tissue to be treated (e.g., tumors). Quality assessment was achieved by imaging (at 1.5 T) a phantom filled with a homogeneous mixture of demineralized water and premixed wallpaper paste. Temperature difference maps were generated by acquiring PRFS phase images before and after RF irradiation, for varying focus positions. Based on this quality assessment, the tested applicator was found to be acceptable for clinical use.

A highly interesting RF applicator system has been presented several years ago (Winter et al., 2013). This design of a hybrid RF applicator supports MRI as well as MR-controlled RF heating at high magnetic fields

(>7 T). The authors provided the experimental proof-of-concept for their applicator for 7 T, and simulations up to 14 T. The applicator is based on an eight-channel transmit/receive system employing a bowtie electric-dipole antenna. Phase-based PRFS temperature difference maps with 0.6 × 0.6 mm in-plane resolution were obtainable, albeit with a 6-mm slice thickness. In tests, RF heating experiments confirmed the predictions of EMF (electromotive force) simulations. Temperature difference maps obtained for an agarose hydrogel phantom and confirmed by temperature measurements with fiber optic probes were very similar to the corresponding simulated maps.

The quality of MRT crucially depends on SNR and temporal resolution of the temperature maps, but the latter are frequently limited by signal detection through one channel only or, in some cases, through just a few (typically four) channels. Chen et al. were able to boost SNR by developing a flexible nine-channel coil array (Chen et al., 2020); see also Table S1. The goal was to enable efficient, high-SNR, real-time parallel imaging (about 3 s between consecutive temperature difference maps) in three dimensions at 3 T. Artifacts due to movements of the imaged object between the acquisitions of the reference phase PRFS map and the maps following HIFU heating by up to 8°C were addressed by using a reference-less sequence that uses the phase information from outside the heated region to estimate the background phase within that region. The performance of their nine-channel design was tested in rabbit muscle *in vivo*. Based on fiber optic probe measurements, temperature accuracy was determined to be superior to results for a classical four-channel design, due to an SNR increase by a factor of 2.6.

When Hyperthermia Alone Is Not Enough: MRT Developments for Combined Treatment Procedures

Hyperthermia alone may not be sufficient for efficient tissue ablation. In particular, the usefulness of hyperthermia may be limited by heat convection in highly vascularized tumors. This results in long sonication times and unpredictable thermal-lesion formation in FUS (Crake et al., 2018, 2017). Therefore, FUS has been shown to be more efficient when used in conjunction with phase-shift nanoemulsions (PSNE). (Note that, in the context of PSNE, the notion "phase" relates to ultrasound, not to magnetization or RF). PSNEs promote cavitation (acoustic droplet vaporization, ADV) at high US intensities and, as a consequence, lead to accelerated tissue heating by way of high-energy bubble collapse. This is achieved by a FUS transducer through (1) a high-amplitude burst producing evaporation, followed by (2) a low-amplitude burst to promote cavitation and temperature rise. Crake et al. have evaluated a combination of MRT (phase-based PRFS) and passive acoustic mapping (PAM, by way of a separate US array) for monitoring the effects of PSNE-enhanced FUS through phantom studies (Crake et al., 2017) and tumor ablation experiments in rabbits (Crake et al., 2018). The use of PAM and MRI together allowed simultaneous mapping of cavitation and the resulting temperature rise, respectively. As a result, the occurrence of cavitation and tissue temperature were positively correlated. The maximum heating assessed from MRI was well correlated with the integrated acoustic emissions over time from PAM, illustrating cavitation-enhanced heating. Tissue examination revealed thermal lesions which were enlarged in the presence of PSNE. Substantial variation in cavitation and heating enhancement between multiple animals pointed to the need for real-time monitoring.

Although the cavitation method discussed in the preceding paragraph is based on a physical effect, there are also chemical effects that may occur in the context of hyperthermia. The most important example certainly is thermoembolization, a technique aimed at occluding blood vessels to starve particular tissue regions (e.g., tumors in the liver) of oxygen and nutrients. Here, an embolic agent is delivered through a catheter to the targeted tissue, in general in combination with cytotoxic drugs. This causes ischemia and nutrient deprivation while also leaving a high local dose of chemotherapeutic drug. The embolic agent acts through an exothermic chemical reaction, such as hydrolysis of dichloroacetic acid chloride. In this way, thermoembolization has both thermoablative and antimetabolic effects. Recently, Fahrenholtz et al. have presented the first *in vivo* test of liver thermoembolization in a swine model and have determined associated temperature changes in explanted kidney using phase PRFS-based MRT (a 2D multiple fast gradient-recalled echo or MFGRE sequence) at 3.0 T (Cressman and Guo, 2018; Fahrenholtz et al., 2019). MRT-measured temperature changes of up to 30°C were found to be within ±1°C of reference values measured through fiber optic probes. Through these experiments, the authors obtained insight into the physicochemistry of thermoembolization by observing spatial heat distribution over time (up to 20 min post injection). Thus, monitoring temperature is expected to gain further information on the details of tissue damage during thermoembolization treatment.

A different form of targeted drug delivery is hyperthermia-triggered liberation of drugs from temperature-sensitive liposomes. For instance, anticancer drugs enclosed in said liposomes are released when, in a well-defined tissue region, temperature is moderately increased to about 42°C (usually by HIFU) after injection of the liposomes. Here, temperature maps generated by PRSF-based MRT enable monitoring of the treatment procedure (Grüll and Langereis, 2012).

Dealing with Misleading Temperature Measurements: Study of Artifacts in MRT

Accuracy and precision of temperature measurement by PRF methods are affected by numerous experimental factors and conditions. On the one hand, tissue-related properties such as the biochemical composition of intra- and extracellular fluids may have a measurable effect on the PRF. Some of the confounding factors present in heterogeneous tissue, as well as newer methods to take these into account, have been discussed above (from the subsection "Avoiding Motion Artifacts by Keeping up with Moving Body Tissue: Acceleration of Thermometric Imaging by Phase-Based PRF" to the subsection "When Hyperthermia Alone Is Not Enough: MRT Developments for Combined Treatment Procedures"). The resulting effects are generally more pronounced for the commonly used chemical shift-based phase temperature mapping technique than for methods based on direct chemical shift determinations and have been aptly reviewed as early as 15 years ago (Denis de Senneville et al., 2005). On the other hand, serious artifacts stemming from metallic implants in the body have been recently analyzed (Weber et al., 2017). In this work, a two-dimensional multi-spectral imaging (MSI) sequence was evaluated and found to significantly reduce temperature errors compared with conventional MRT, in particular when used in conjunction with T_1-based thermometry. MSI is a single-shot fast spin echo technique based on excitation of finite spectral and spatial regions. In this sequence, which is an advanced version of a previously published inhomogeneity correcting sequence (Cho et al., 1988), an additional slice selection gradient is applied after the first one (used for excitation), but with inverted gradient magnitude, which in turn is followed by a refocusing gradient. The shapes of the RF pulses during excitation and refocusing are chosen such that the overlap of the slice profiles for excitation and refocusing yields the profile of a frequency bin for which field inhomogeneity effects are canceled out. The frequency bin selected in this way then determines the spatial origin (voxel) of the signal detected. The experiment is then repeated with different combinations of RF pulse shapes to shift the origin of the voxel as a function of the desired spatial resolution, without the necessity for phase encoding steps. The low sensitivity of this spatial selection technique to field inhomogeneity makes it suitable for acquiring images with minimal distortions due to susceptibility effects caused by metallic devices. The authors achieved a 1.9-mm in-plane resolution at 3 mm slice thickness and a temporal resolution of 5 min at 3.0 T in a 2% agarose gel phantom with a titanium or cobalt-chromium-molybdenum alloy shoulder replacement implant inserted. Temperature mapping was achieved via T_1 mapping through preparation of the MSI sequence with an inversion-recovery sequence with varying inversion times. In parallel, temperatures were independently verified by fluoroptic temperature probes at selected positions in the phantom. The resulting temperature uncertainty was determined in calibration experiments and was found to vary between 0.8°C and 1.4°C. Comparison with PRFS thermometry showed that, although the PRFS method is generally more accurate and precise than T_1-based thermometry, the latter is more reliable in the presence of strong susceptibility effects in the vicinity of metallic objects.

Double-Checking Temperature Measurements: Calibration and Confounding Factors in MRT

It has been well known for many years that the water proton chemical shift of an aqueous solution is influenced by its (bio)chemical composition, in particular by its metabolite and serum content. This has led to the conclusion that, for exact temperature measurement by PRF methods, calibration curves need to be based on solutions that appropriately reflect the conditions of the biological environment to be studied (Lutz et al., 1993). For instance, Vescovo et al. have carefully studied effects of ionic strength and protein content on calibration, with the aim of providing accurate temperature values in brain tissue on the basis of the chemical shift of water protons relative to that of NAA methyl protons at 1.5 T, as measured by ^{1}H MRS (Vescovo et al., 2013). The authors designed a complex phantom guaranteeing stable temperatures between 20°C and 45°C over long periods and used a fluoroptic probe for the determination of "ground truth" temperatures. They also employed a statistical approach to compare the accuracy of their calibrations with those from other groups and found systematic deviations in some cases.

More recently, Verius et al. obtained temperature calibration curves from phantoms (phosphate-buffered metabolite solutions) by using not only NAA methyl protons but also methyl and methylene protons of creatine (Verius et al., 2019). They compared *in vivo* human brain temperature values based on ^{1}H MRS with

results provided by an infrared ear thermometer that also served to measure the phantom temperatures during the calibration experiments. This study primarily stressed the influence of MRI hardware and software, including software for spectrum evaluation, on accuracy and reproducibility of absolute temperature. Both NAA and Cr methyl peaks were found to be appropriate for obtaining reliable *in vivo* temperatures but not the Cr methylene resonance.

To render tests of noninvasive thermometry in hyperthermia conclusive and ensure its widespread use in the clinic, it is vital to subject this relatively new method to multi-institutional evaluation. One such quality assurance study has been presented for deep-pelvic MW hyperthermia systems operating in multi-vendor MR-systems, using a new anthropomorphic phantom (Curto et al., 2019); see also Table S1. These authors have systematically compared hyperthermia-induced temperature variations to values obtained by invasive temperature probe measurements using high-resistance thermistors, the current gold standard. Although the phantom used was filled with a rather conventional agar gel, the shape of the phantom shell had been designed to mimic an anatomical body with bone structures. The bone-mimicking structures were made of materials with known permittivity (electric polarizability) and electrical conductivity. The dielectric properties of the phantom filling were also determined. 3D MR thermometric phase-based PRFS images based on GRE sequences were obtained at 1.5 T, with varying acquisition parameters. Differences between thermistor and MRT-measured temperature increases were consistently below 1°C in this setting. This successful multi-institutional quality assurance work should facilitate MRT becoming the new gold standard, replacing the invasive thermistor method.

Nearly all biomedical MRT methods were originally developed to measure the thermal response of tissue to heating by medical devices, i.e., to different forms of therapeutic hyperthermia. However, a question to be raised in this context is whether the measurement of such tissue temperature variations may be confounded by temperature changes due to physiological factors. Apart from the trivial influence of fever on body temperature, little attention has been paid to this issue. Rango et al. have recently presented a study of potential brain warming upon activation of the visual cortex (Rango et al., 2015). During a 6.5-s visual stimulation, no significant temperature changes were observed for 20 normal subjects; however, during the first 3 s of recovery, a temperature increase by 0.6°C was detected, followed by a return to pre-stimulation temperature (standard deviation given as 0.2°C). All (absolute) temperature values were obtained from single-voxel ^{1}H MRS of the brain region in question, as well as a control region (centrum semiovale). As a consequence, neuronal firing did not seem to result in a temperature increase, but the first seconds following neuronal firing appear to be characterized by minor heat release. In summary, although the stimulation of the virtual cortex may result in blood oxygenation level-dependent MRI effects and metabolic changes, its effect on tissue temperature clearly is of a smaller order of magnitude than that caused by clinical hyperthermia.

THE LEADING MRT APPLICATION: TEMPERATURE MEASUREMENT IN MR-HIFU HYPERTHERMIA

The section "The Methodological Groundwork: Advances in MRS and MRI Temperature Methods" focused on general methodological aspects of MRI thermometry relevant to various actual and potential applications, notably addressing various hardware and software-related technical and instrumental issues, whereas the next three sections will be dedicated to specific MRT applications per se, including application-specific adjustments.

Destroying Tissue by Heating with Ultrasound: MRT Applications in Tissue Ablation

As outlined the Introduction section, the most prevalent use of MRI thermometry occurs in conjunction with high-intensity focused ultrasound, the combination of these two techniques being known as MR-HIFU (or MRgHIFU or MRgFUS). The most relevant clinical applications of this approach concern tissue ablation, mostly in the context of tumor treatment. Brief overviews of this group of applications, directed to clinicians, have been published in the past decade, hinting at brain, breast, prostate, and liver tumors as the primary targets (Colen et al., 2017; Cornud et al., 2018; Siedek et al., 2019a, 2019b). It has also been pointed out that thermal ablation of nonneoplastic central nervous system tissue is a valid option, e.g., for patients suffering from chronic neuropathic pain (thalamotomy). In the following, we deal with the most recent developments in tissue ablation MRI thermometry in more detail.

When used to ablate brain tissue, HIFU is often limited by the calvaria as the skull reduces ultrasound penetration. MacDonell presented a device for interstitial HIFU to be used in conjunction with real-time MRT

(MacDonell et al., 2018). This invasive system leads to shorter sonication times and allows for the use of tailored heating patterns providing precise ablation margins regardless of tumor shape, location, and proximity to blood vessels. In addition, biopsy can be performed concurrent with treatment. (This application demonstrates that in current hyperthermia treatment protocols, the heating technique used, and not MRT, may be the speed-limiting factor.) Consequently, MRI providing real-time feedback was used in conjunction with a HIFU-administering MRI-compatible robotic assistant akin to a stereotactic frame (magnetic resonance guided robotic assistant, MRgRA). The MRgRA inserted the HIFU probe by way of a 13-gauge implant catheter; the minimally invasive cannula was of interest also due to its diagnostic capabilities (biopsy). The authors demonstrated their proof of concept in an animal modal (pig).

A different way of improving the definition of ablation regions has been proposed by Ozhinsky et al. for prostate treatment with a rectal transducer probe (Ozhinsky et al., 2018); see also Table S1. The goal of their study was to develop an MRT-guided platform based on a commercially available prostate array (ExAblate, 2000) that would achieve uniform stable heating over large volumes within the prostate. Here, it was important to enable the user to precisely control the power deposition patterns and the shape of the region of treatment. During sonication of a tissue-mimicking phantom, temperature difference maps (phase PRFS) were created in real time using a spoiled gradient echo (SPGR) sequence at 3.0 T. Based on these images, the HIFU controller module determined repeatedly which of the HIFU spots was the coldest, in order to use that spot as the focal point for the next HIFU sonication period. In this way, the authors were able to reach the target temperature (7.5°C above the starting temperature) within 4 min and kept the temperature stable at that value for at least 6 min.

Ablation of abdominal tissue is complicated by respiratory motion since the spot to be treated by HIFU is not stationary. In fact, motion tracking is required to ensure an optimal tissue temperature profile. Lorton et al. have developed a real-time hybrid US-MR imaging approach for self-scanned HIFU ablation of moving tissue (Lorton et al., 2019). Motion detection and tracking is achieved by US-based speckle imaging (short exposures). This is a technique tracking temporal shifts in the backscattered US signals resulting from the displacement of tissues (Petrusca et al., 2012). The resulting speckle images serve two purposes: (1) to adapt on-the-fly the RF and gradient pulses of the MRT sequence such that the field of view follows the movement of the selected slice (segment-based slice following), and (2) to modulate the HIFU power based on the calculation of tissue speed. The overall goal is to compensate for the effect of tissue motion on the thermal build-up. Although preceding methods using motion compensation in HIFU ablation were based on electronic steering of the US beam (Celicanin et al., 2018), the new technique suggested by Lorton et al. keeps the US beam and, therefore, the focal HIFU spot static, but modulates US power as a function of tissue position relative to the US beam. The performance of this new method was tested experimentally, using *ex vivo* turkey breast tissue. Uniformity of the resulting temperature profiles was assessed through 2D phase PRFS images under conditions of both periodic and non-periodic (breathing-like) sample motion. Temperature difference images obtained resulted in the first experimental validation of the self-scanning HIFU ablation paradigm via real-time hybrid MRI/US imaging. Future *in vivo* tests of this method should reveal its usefulness for practical medical purposes.

Advantages and disadvantages of different ablation techniques have been discussed in a recent overview (Zhu et al., 2017). Among these, ultrasound ablation stands out as a particularly practical technique because it combines three clinically important features: (1) MR compatibility; (2) the ability to focus the area of treatment without direct contact, combined with good depth penetration; and (3) absence of tissue charring upon ablation. Consequently, MR-guided HIFU applications experienced much faster development than alternative MR-guided techniques. Nonetheless, examples of the latter will be discussed in sections Of Particular Clinical Interest: Temperature Measurement in RF and MW Hyperthermia and Healing with Light: Temperature Measurement in LITT and PDT Hyperthermia.

Keeping Mild Ultrasound Hyperthermia under Control: MRT for Better Targeting Diseased Tissue and Protecting Surrounding Tissue in Non-ablative Applications

Development of new hyperthermia protocols frequently relies on tests in experimental animals. Two recent papers presented developments specifically designed for application in small animals. Bing et al. addressed the particular challenge of small target size in mild hypothermia of experimental animals (Bing et al., 2015); see also Table S1. Their MR-compatible HIFU system, adapted for use in a clinical 3.0-T MR imager, consists of a dedicated ultrasound transducer with sector-vortex lenses and

a custom-made receiver coil (surface coil). Tissue-mimicking phantoms and a rat model were tested for 30-min mild hyperthermia followed by a 10-min cooling period. The RF coil enabled acquisition of temperature maps with a 1 × 1 × 1.5 mm voxel size and a temperature uncertainty of <0.5°C. Abraham et al. tested several different coil designs embedded in an ergonomic mouse treatment bed mounted in a water-filled FUS treatment tank (Abraham et al., 2018); see also Table S1. The coils investigated included several transmit/receive coils of different diameters and a combination of a half-bird-cage transmit coil with a surface receive coil. Precise and accurate temperature results were obtained at 3.0 T, thanks to the increased B_1 homogeneity achieved by the half-bird-cage transmit coil, which resulted in highest SNR values. Temperature mapping was investigated *ex vivo* on fresh chicken breast tissue and on mouse cadavers. The authors indicated that further fine-tuning of their protocol may be needed to minimize overshoot.

Tumors to be treated with mild hyperthermia may involve deep tissue targets, e.g., recurrent rectal cancer in enhanced radiation therapy and chemotherapy. Chu et al. provided a preclinical validation of MR-HIFU hyperthermia for this application, followed by a clinical imaging study, both obtained using a 3.0-T system (Chu et al., 2016). For the preclinical study, a swine model was employed. Targets were chosen (1) deep in thigh muscle to examine the attainable treatment depth and (2) at the rectal wall to examine thermometry quality when using rectal ultrasound filling to stabilize peristaltic motion. The thigh muscle experiment resulted in a phase PRFS-measured temperature uncertainty of 0.3°C (for four sonications, and temperatures between 41°C and 43°C for 30 min) as ascertained by a fiber optic probe, and in a heating uniformity in the target region, an 18-mm ring, with a temporal average of 1.4°C and a maximum of 2.3°C (at a maximum depth from the skin of 80 mm). MRI temperature measurements near the rectal wall matched the implanted fiber optic sensors to within 1°C without rectal filling and within 0.2°C with rectal filling to reduce thermometry artifacts caused by peristaltic movement. For the clinical study, six volunteers with biopsy-proven primary rectal cancer were chosen. For measurements in these patients, temperature imprecision was unacceptable (7.8°C) without rectal filling and satisfactory (1.1°C) with rectal filling. However, the authors derived absolute temperature values from phase-based PRFS values by using a fiber optic probe-measured temperature, obtained at the start of each experiment, as a reference (baseline temperature). Thus, the tacit assumption was that this baseline temperature was also valid for PRFS-monitored tissue regions distant from the tip of that probe, i.e., that the baseline body temperature is entirely uniform, which may not always be the case. This determination of a baseline temperature also implies that the values given for differences between PRFS and fiber optic-probe temperatures, observed in the course of the experiment, were not based on truly independent measurements since the PRFS values had originally been calibrated using the initial fiber optic-probe value as a baseline. In a nutshell, the PRFS-derived absolute temperature values presented in this work should be considered rough estimates rather than measured results and would be entirely inaccessible in clinical situations where fiber optic probes cannot be inserted into the tissue to be subjected to hyperthermia.

An additional, very recent paper dealt with motion effects in abdominal phase image-based PRFS thermometry (Tan et al., 2019); see also Table S1. These authors suggest the use of a combination of two previously developed methods, principal component analysis (PCA) and projection onto dipole fields (PDF), abbreviated HPP (hybrid PCA-PDF). HPP was tested in *in vivo* porcine kidney (with moderate sonication for 25 s at 90 W) and in human volunteers (without heating). For all human and porcine subjects analyzed, HPP achieved an overall mean pixel-wise temperature standard deviation of 0.86 ± 0.41°C, which was substantially lower than three alternative correction methods tested.

A sophisticated method for prediction of spatiotemporal liver motion, based on partial motion observations, has been validated by Tanner et al. *in vivo*, in the context of MRT (Tanner et al., 2016). This technique is a tracking method based on MR images routinely acquired during MRgFUS and has been designed to be used in freely breathing patients. To create a motion model, 4D-MRIs were acquired for 16 volunteers (three spatial dimensions, one temporal dimension). This was achieved by way of an interleaved sagittal 2D sequence generating numerous images over many breathing cycles, with slices covering the liver, alternating with a navigator slice. Prediction accuracy was determined with respect to manually annotated landmarks. MR tracking had a mean accuracy of 1.1 mm, and motion of the liver was spatiotemporally predicted with an accuracy of 1.9 mm (clinical requirement: 2 mm) for a latency of 216 s, by a model based on (1) individualization using a 3D breath-hold image and (2) tracking liver vessel motion on 2D thermometry images.

Providing Stability and Safety in Mild Hyperthermia Using Ultrasound: MRT in Particularly Challenging Non-ablative Applications

Apart from physical motion of the tissue area to be sonicated, also gradual fluctuation of the center frequency of the MRI scanner may present an instability affecting the precision of MRT and hyperthermia treatment. These fluctuations are due to environmental changes (magnetic-field drift) and dynamic temporal and spatial magnetic-field variations owing to heating of magnet components during scanning. Bing et al. have developed a retrospective drift correction algorithm to counter such effects (Bing et al., 2016); see also Table S1. The retrospective drift correction algorithm used a slice-by-slice DC correction of changes in the main magnetic field strength, combined with a 3D first order correction of changes in the spatial distribution of the main magnetic field. The retrospective corrections were based on phase drifts observed in image regions of interest that remain at a fixed temperature during the heating experiment. The performance of the proposed correction strategy was first evaluated *in vitro* in a phantom, with fiber optic probes inserted for the determination of ground-truth temperatures. Subsequently, an *in vivo* evaluation was performed for mild hyperthermia treatment with MR-HIFU (phase-based PRFS) over up to 40 min in a rabbit model (temperature generally maintained within the range of 41°C–43°C, occasionally up to 45°C). The combination of correction techniques resulted in a clinically acceptable temperature error of 0.57°C in the heated region, and 0.54°C in the non-heated region, down from about 15°C without any correction.

Temporally stable and spatially even temperature distribution within a well-defined region of interest is of extreme importance in applications such as hyperthermia-mediated drug release from thermosensitive liposomes. Staruch et al. have carefully measured multiple thermal parameters during an MR-HIFU experiment over a 20-min heating period in a rabbit thigh tumor, concomitantly with thermosensitive liposomal doxorubicin (TLD) treatment (3-T MRI system, with an ultrasound transducer built into an MRI patient bed) (Staruch et al., 2015). The thermal parameters included the temporal mean of the spatial median (T50), and the temperatures that 10% or 90% of the target region exceeded (T10 or T90, respectively), in different slices through the heated target volume. The MR-HIFU ultrasound focus was steered electronically using a feedback control algorithm, where the input for feedback control was the mean temperature measured in voxels within the target diameter on slices defined across the ultrasound focus. Starting from a baseline temperature of 34°C, the maximum temperature reached during heating was 42°C (T10), whereas T50 and T90 were at 41°C and 39.8°C, respectively, and varied temporally with a standard deviation of 0.4°C over the treatment duration. Temperatures sufficient for drug release ($\geq$40°C) were reached within the target volume after 2 min of sonication, which is when 5-min intravenous drug injection began. The T90 and T10 values indicated that the spatial uniformity of heating was sufficient to ensure drug release in the entire target region. Consequently, the authors found that tumor treatment with TLD was more efficient with than without MR-HIFU sonication (markedly decreased tumor volumes and increased survival for animals at day 60 post treatment).

Besides technical, biological, and medical issues, mild-hyperthermia MRgHIFU also requires consideration of safety questions, in particular in the context of heating targets located in a heterogeneous space with moving organs and fluids such as the pelvis. Here, controlled heat delivery over extended durations of hyperthermia to a region with inhomogeneous thermal properties is a major challenge. Therefore, Zhu et al. evaluated the feasibility and safety parameters of using MRgHIFU to moderately heat an array of different tissue geometries in the pelvis to $\leq$44°C through ultrasound exposure (1 MHz, 100 W) (Zhu et al., 2019). The authors tested a maximum focal depth of 8 cm in a pig model using an EPI-based phase PRFS thermometry method. However, prior to the *in vivo* experiments, MRT sequences were run on a commercially available MRgHIFU quality assurance phantom. In addition to the assessment of temperature mapping accuracy, precision, temporal variation, and heating uniformity, several parameters linked to thermal damage were determined. These comprised the detection, by contrast-enhanced MRI, of abnormally perfused tissue in the hyperthermia target region, readily distinguishable from ablated regions and hemorrhage. Histological analysis was able to distinguish, among other features, reversible tissue damage (mild congestion in particular muscles; accumulation of white blood cells) from irreversible tissue damage (no occurrence of the latter) along with T_1-weighted MRI. The average temperature accuracy was better than 0.8°C, and thus sufficient for clinical applications. In conjunction with adequate heating uniformity and the absence of spots above the desired temperature range, mild-hyperthermia MRgHIFU was found to be feasible in a safe way in heterogeneous spaces.

OF PARTICULAR CLINICAL INTEREST: TEMPERATURE MEASUREMENT IN RF AND MW HYPERTHERMIA

Supervising Electromagnetic Tissue Destruction: Temperature Control in Heart, Liver, and Skeletal Muscle

Although MR-HIFU is by far the most popular method for heat-based tissue ablation, RF (upper kHz and low/intermediate MHz frequency range) and MW (upper MHz and GHz frequency range) ablation have found important applications where ultrasound-based ablation would yield inadequate results. Ozenne et al. have recently presented an improved MRT method for monitoring lesion formation during cardiac catheter ablation by RF (Ozenne et al., 2017); see also Table S1. The specific challenge one faces when trying to obtain real-time temperature maps of heart tissue consists in the necessity to achieve a clinically meaningful spatial resolution under conditions of both respiratory and cardiac motion. The authors were able to increase spatial resolution approximately 5-fold (based on voxel size) by using electrocardiogram-triggered EPI associated with parallel imaging (GRAPPA) and motion correction using an optical flow (OF) algorithm. This new concept was tested at 1.5 T on a sheep, with one catheter (right ventricle) for cardiac pacing and a second catheter (left ventricle) for ablation. Humans (volunteers) were only used to assess temperature stability under free breathing conditions. It was shown that the temperature distribution in the myocardium during free breathing in humans can be mapped with only 1°C of uncertainty, at an update rate given by the cardiac cycle (~1 s), and an in-plane spatial resolution of 1.6 mm × 1.6 mm (3 mm slice thickness). Thus, the proof of concept for a potentially clinically relevant MRT method during cardiac catheter ablation has been provided.

Mukherjee et al. reported the feasibility of performing epicardial voltage mapping and RF ablation under real-time MRI guidance in a porcine model (Mukherjee et al., 2018). As in the work described in the preceding paragraph, phase-based PRFS thermometry was employed (Figure 8), but with a somewhat lower spatial resolution (1.6 mm × 1.6 mm in-plane, and 5 mm slice thickness). Although Mukherjee et al.'s work makes available important additional MRI-guided information (epicardial voltage) in conjunction with MRT and lesion imaging, it is more limited than Ozenne et al.'s method from a pure MRT point of view. Mukherjee et al. did not (1) make use of a fully automated pipeline, nor did they (2) assess the sensitivity and specificity of MRT. However, integration of the letter techniques should be possible also in the presence of epicardial voltage mapping.

Robust thermometry of the liver is particularly challenging, in view of the target location deep inside the body. The practical implementation of some required modifications to equipment and workflow, taking into account the significant clinical constraints in the context of clinical MR-guided MW ablation, was presented recently (Gorny et al., 2019); see also Table S1. The most important modifications made concern the addition of RF filters (chokes) to the MW generator's coaxial lines and electrical grounding of the MW generator through copper wool. All experiments were performed on a 1.5-T clinical MRI scanner, using a standard clinical MW ablation system. Tests were carried out with a saline phantom; then, the optimum design was used in liver tumor ablation patients, in all cases with the MW antenna inserted into the object to be irradiated. The overall uncertainty in temperatures found in patient data was on the order of ± 1.4°C. Although this study has identified and eliminated several sources of avoidable temperature errors, further optimizations would be needed to keep the temperature below 1.0°C. Most likely, critical factors in this regard are compensation of field drift, inclusion of fat suppression in MRI, and taking into account tissue motion.

Another interesting application of MR-guided RF ablation involved a single loopless antenna used for RF irradiation as well as temperature difference mapping by phase PRFS (Ertürk et al., 2016). An RF switch has been designed that enabled the operators to switch between ablation and imaging. The presence of an RF antenna localized at the site of ablation permitted acquisition of images at a very high spatial resolution (0.3 mm × 0.3 mm in-plane, and 2 mm slice thickness) and to closely integrate orientational imaging with heat delivery, temperature difference mapping, and T_1-based relaxation mapping for ablation control. This minimally invasive approach was tested *in vitro* (bovine muscle) and *in vitro* (porcine and rabbit aortas) on a 3.0-T magnet (RF of 128 MHz).

While the preceding paragraph dealt with MW hyperthermia experiments on animal models at relatively high magnetic fields, there is also a need for MW hyperthermia applications at particularly low fields. High-field MR devices are usually closed-bore magnets owing to the requirements of robust shielding

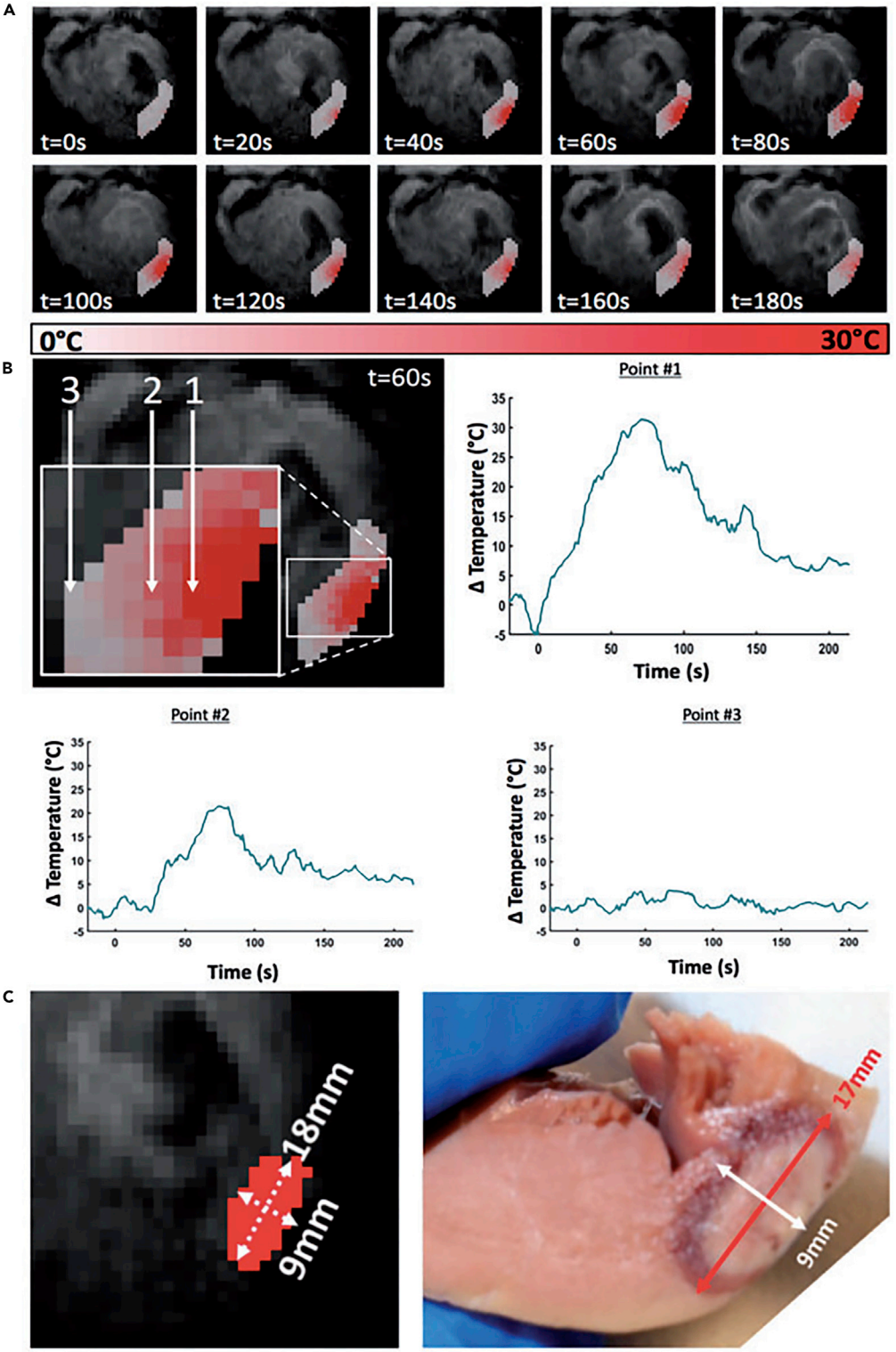

Figure 8. Epicardial RF Ablation Guided by Real-Time Phase PRF MRT: Preclinical Feasibility Study in a Pig Model

In vivo temperature difference maps (A) shown at different time points relative to the start of RF heating. Localized temperature elevation can be clearly visualized on the epicardial side of the left ventricle. (B) Time courses of temperature differences for three selected voxels (indicated by pixel points #1 to #3 in the top left image of this panel), obtained using cardiac MR thermometry during epicardial ablation in swine. A maximum temperature elevation of 30°C–35°C was

Figure 8. *Continued*
observed for a voxel within 2 mm of the RF catheter tip, Point #1 (in comparison with a more remote voxel in myocardium, Point #2). No significant temperature elevation was observed for a voxel located in a very remote area, Point #3. 2D lesion dimensions measured using MR dosimetry (C) correlated well with measurements by gross macroscopy with mild overestimation of lesion width.
Reproduced from Mukherjee et al. (2018), no permission required.

and gradient structure to maintain magnetic-field homogeneity. By contrast, open systems are more suitable for interventional hyperthermia procedures that require easy access to patients. Open-configuration MR scanners are characterized by lower fields (<1 T) and also involve a lower purchase price and reduced operational cost compared with high-field instruments. Therefore, Chen et al. showed by *in vitro* experiments with phantoms and porcine liver that MRT based on drift-correction phase PRFS with first-order polynomial fitting can be applied to monitor temperature changes during MW ablation in a low-field (0.35 T) configuration whole-body MR scanner designed for applications in humans (Chen et al., 2018). However, work on high-field PRFS (cited above) consistently indicated that discrepancies between PRFS and fiber optic probe-measured temperatures are on the order of $\leq 1°C$, whereas errors may increase to about 2°C for fields as low as 0.35 T (Chen et al., 2018). Phase PRFS tests *in vivo* on volunteers showed that drift correction had a marked effect on the stability of temperature measurements in the human brain, setting the stage for future clinical tests involving MW hyperthermia.

Facing Unstable Conditions in Mild RF Hyperthermia: Optimization of Non-ablative Treatment with MRT

Temperature changes under conditions of moderate RF hyperthermia at 100 MHz have been monitored by Hartmann et al. through MR spectroscopic thermometry for deep-seated tumors in the presence of fatty tissue (Hartmann et al., 2017). The authors decided not to employ the widely used PRFS method based on phase images because the latter only allows one to measure relative temperature changes occurring between two separate image acquisitions but not absolute temperatures. This poses a problem in the presence of patient motion or magnetic-field drift between the two acquisitions. The spectroscopic PRF method (single-voxel MRS) enables the spectroscopist to selectively evaluate the chemical shift of the tissue water resonance, without any contribution from the fat methylene resonance. The latter is only used to serve as a chemical-shift reference for the water resonance since its chemical shift is temperature invariant. The authors tested several peak analysis methods for water proton resonances obtained from phantoms consisting of mayonnaise or pork at 1.5 T; peak fitting based on Lorentzian line shapes (MATLAB software) proved to be superior to other methods. Phantom areas were RF heated, and the ensuing temperature increase was monitored for selected voxels (typically 8 cm^3) using the chemical shift of the water proton resonance. Temperatures determined in this way were compared with reference temperatures measured with Bowman probes, i.e., with miniaturized thermistors (resistors the resistance of which is dependent on temperature). The uncertainty in temperature measurement in these experiments was determined to be about 1°C.

HEALING WITH LIGHT: TEMPERATURE MEASUREMENT IN LITT AND PDT HYPERTHERMIA

Modeling Laser Light to Eradicate Diseased Tissue: MRT-Based Temperature Maps for Treatment Planning

Accurate targeting and optimal heat delivery are crucial for successful tissue ablation and for minimizing side effects in hyperthermia. The relevant parameters can be modeled, and the resulting model can be included in treatment planning. One approach to achieve this is predictive modeling of LITT ablation dynamics, as suggested by Jermakowicz et al. for brain tumors (Jermakowicz et al., 2019). The authors suggested the use of three types of preoperative MRI (T_1 imaging with gadolinium-based contrast agent, T_2 imaging, and perfusion imaging), providing predictive features that could be used to improve clinical efficiency with which LITT is delivered to brain tumors. However, this modeling approach alone was not deemed satisfying as it did not include one of the most important factors in LITT ablation, namely, heat delivery. In hyperthermia treatment through MR-guided LITT (MRgLITT), the quality of prediction of tissue ablation critically depends on the use of accurate optical attenuation coefficient values for the tissue under consideration (Mitchell et al., 2018). In spatially heterogeneous tissue, notably in the brain, more than one attenuation coefficient should be considered as a function of the contribution of vessels (blood) and ventricles (cerebrospinal fluid, CSF) to the targeted brain region. This is of particular importance since blood

vessels and CSF represent unpredictable heat sinks for laser-induced heat transfer, unless tissue heterogeneity is taken into account in treatment planning. Therefore, Mitchell et al. have suggested the generation of heterogeneous tissue models for ablation regions of interest (Mitchell et al., 2018). Such a model is based on the segmentation of four distinct tissue types in a laser fiber-locating T_1-weighted MR image. Then, optical attenuation coefficient values were assigned to the distinct tissue labels, and the average optical attenuation coefficient over the photon path from the light source point was calculated. Ultimately, a temperature map was modeled using model parameters optimized by a complex mathematical algorithm. This map was designed to take into account the different tissue properties, with ablation being predicted for regions with maximum temperatures $\geq$57°C. The authors trained the modeling prediction of this algorithm using measured MRT imaging data from actual MRgLITT brain lesion ablations in 22 patients. They demonstrated the superiority of the heterogeneous-tissue versus homogeneous-tissue model, with a temperature measurement inaccuracy of <1°C. However, it is unclear in all cases how the authors derived absolute temperature values from the temperature difference values accessible through phase-based PRFS.

The importance of combining MRI thermometry with simulation methods, notably for the prediction of temperature rise and the coagulation zone, has prompted Bazrafshan et al. to develop a dedicated software tool for monitoring LITT (Bazrafshan et al., 2019; Hübner et al., 2017). This simulation is based on radiation and heat transfer in biological tissues, in particular for liver ablation. The MRT sequence of choice was phase PRFS (with EPI), as this method is considered the gold standard for fast clinical temperature mapping. The authors evaluated their approach using MRgLITT of *ex vivo* pig liver at 1.5 T and simultaneously measured temperature through a fiber optic "thermometer." The imprecision of the MRI temperature amounted to 2.4°C. Although this appears to be a relatively large uncertainty, it reflects the fact that the temperature-sensing tip of the fiber optic probe reports the temperature within a very small tissue volume, whereas any PRFS-determined temperature necessarily comprises a somewhat larger volume. The achievable precision was deemed sufficient for the purpose of efficiently predicting and controlling tissue ablation.

Studying Thermal and Structural Properties of Materials under the Influence of Laser Light: MRT Studies on Phantoms and Tissues

Although the modeling procedure described in the preceding paragraphs required elaborate mathematic algorithms, a more empirical approach was chosen to predict the heat distribution and heat effects in LITT in spatially less heterogeneous tissue (here: the prostate). For this purpose, Geoghegan et al. developed phantom material matching the optical and thermal properties of the human prostate (Geoghegan et al., 2019). The phantoms tested consisted primarily of a polyacrylamide-based hydrogel because of its high melting point and optical transparency, and its optical properties were further optimized by an appropriate dye (Naphthol Green B) and a micellar aqueous solution (Intralipid). For the purpose of mimicking protein coagulation, BSA and citric acid were added. The authors performed comprehensive assays to optimize the concentrations of the compounds used, including a special mix of initiators for acrylamide/bis-acrylamide polymerization. The purpose of this optimization work was to find the best possible match with human prostate tissue values for the optical scattering coefficient, the absorption coefficient, thermal response, and coagulation, with the coagulation zone conveniently identified by T_2-weighted MRI using a 3-T scanner. Phantoms were subjected to heating by LITT (laser light at 980 nm wavelength), and MRT maps (phase-based PRFS method) were generated during the process, while (absolute) reference temperatures were determined simultaneously by way of a fiber optic probe located at the LITT region of interest. Comparable results were obtained for this phantom and patients' prostates. Although the specific advantage of the phantom is its homogeneity and reproducibility, it lacks the perfusion present in human tissue before necrosis induction, and also *in vivo* anatomical factors. Therefore, this phantom was not recommended for direct pretreatment planning, but as a platform for the development and optimization of LITT tools and techniques including probes and MRT.

A different and much more basic phantom material was used by Odéen et al. for developing, testing, and evaluating improved 2D and 3D protocols for phase-based PRFS imaging of LITT at 1.5 and 3.0 T (Odéen and Parker, 2019b); see also Table S1. These authors employed tissue-mimicking Gellan gum gel, a polysaccharide hydrogel known to be more stable than agar gel under conditions of elevated temperature. First, temperature precision was determined for the human brain for different RF coils (head, body, and flexible multi-channel coils). Best precision (0.19°C uncertainty) was obtained for posterior head and flexible coils at 3.0 T, for a 2D GRE sequence with four echoes. The same experimental parameters allowed for

even better precision (0.08°C uncertainty) in phantom measurements, where the inaccuracy of temperature measurements was 0.17°C judged by simultaneous thermometry with an optic fiber probe. Although the 3D EPI methods employed resulted in somewhat increased errors for accuracy (best phantom value achieved: 0.31°C, for 0.19°C imprecision), these results represented substantial improvements over values previously obtained for LITT 3D thermometry protocols.

In the preceding paragraphs of this subsection, and in the previous subsection, the role of coagulation in ablative hyperthermia through LITT has been emphasized. Coagulation is one indicator of successful tissue damage caused by heat, but it is desirable to obtain, in real time, overall thermal damage estimates (TDEs) in order to precisely control LITT in well-defined tissue regions. Commonly, this is achieved by MR-generated thermal maps indicating the spatial distribution of temperature increases during the treatment procedure. However, a substantial proportion of post-treatment damage maps, frequently obtained through T_1-based MRI, indicated the existence of discrepancies between intraoperative MRT-derived TDE images on the one hand and post-treatment T_1-based maps on the other, in particular for cases where TDE maps had been calculated from MRT maps that exhibited characteristic artifacts (central signal voids). These discrepancies concern size and shape of ablative areas. Although the origin of these artifacts is not entirely clear at present, Munier et al. quantified their effect on the precision of intraoperative assessment of ablative areas for a group of patients undergoing intracranial MRgLITT (Munier et al., 2020). They found that the statistical correlation between the two measures of ablative areas was weaker for TDE maps obtained from artifact-containing MRT maps than for TDE maps from artifact-free MRT maps. The factors contributing to these artifacts, as well as the question of the clinical relevance of the resulting uncertainty, remain to be studied.

Measuring Light by Measuring Heat: MRT Applied to Phototherapy

In all applications discussed up to this point, the final physical parameter to be determined by MRT was temperature. This is consistent with the general purpose of monitoring tissue heating during controlled hyperthermia treatment. However, there are other heat-generating forms of treatment involving, for instance, particular forms of light irradiation, the primary purpose of which is not heat delivery to the tissue but the initiation of specific chemical and biochemical reactions. This is the case in PDT, where an injected compound, the photosensitizer, absorbs light and subsequently triggers the production of various reactive oxygen species (ROS); these ROS are purposely produced to damage tissue, notably in cancer treatment. Here, the physical parameter of primary interest is not temperature, but the optical fluence rate, a measure of the local intensity of light. In all cases where the fluence rate is significantly correlated with temperature increase, the latter can be used to determine the former (Schreurs et al., 2017). The specific value of this approach derives from the fact that there currently is no direct noninvasive method available for measuring the tissue fluence rate, whereas knowledge of this parameter is of great interest for predicting the efficiency of PDT. Schreurs et al. have demonstrated that spatial-temporal temperature data (temperature change maps) generated by MRT (phase-based PRFS) can be used to construct fluence rate maps by dividing the heat data by the tissue absorption coefficient (Schreurs et al., 2017). This was shown by way of simulations using virtual MRT datasets based on analytically described fluence rate distributions, which was tested experimentally in gel phantoms containing Evans Blue. The suggested technique was also applied *in vivo* in a mouse model. First, a dynamic series of phantom temperature difference maps was generated before, during, and after irradiation by laser light at 655 nm wavelength. From these maps, time derivative maps and maps of the second derivative (Laplacian) were obtained by calculating the analytical derivative of local polynomial fits, performed at each pixel and each time point. The fluence rate map was then calculated using the established heat diffusion equation and by dividing the resulting light-induced rate of heat energy by the separately determined phantom absorption coefficient as indicated above. In the phantom and animal experiments, MRT-determined fluence data were compared with results obtained with a classical fluence rate probe consisting of a ceramic spherical bulb mounted onto the distal end of an optical fiber. The bulb was located close to the light source, i.e., near a diffuser at the end of a second fiber connected to the 655-nm laser. A significant linear relationship was obtained between the two independently determined fluence rates ($\rho = 0.896$, $p = 0.0026$). In this way, MRT has evolved into a useful tool for assessing, e.g., the dose-response relation in PDT, and it may also play a role in fundamental biomedical optics research.

MEET THE COMPETITION: MAGNETIC RESONANCE-BASED VERSUS ALTERNATIVE TEMPERATURE METHODS

Although MRT by various PRF methods is the established gold standard for monitoring clinical hyperthermia treatment noninvasively, this approach is not without competition from non-MR techniques. For instance, Karwat et al. suggested to determine the "temperature distribution" in tissue using the phase shift of ultrasound echoes (PSUE) (Karwat et al., 2016); see also Table S1. This method was specifically developed for cases where hyperthermia is applied using HIFU treatment. Here, the hypothesis is that ultrasound can be used for both hyperthermia localization and hyperthermia treatment and would thus render the relatively expensive MRT equipment obsolete. The physical background of the suggested method is the temperature dependence of sound velocity in most biological tissues (with the exception of fat). This relationship is linear within the pre-ablative temperature range (up to 43°C). The authors presented the mathematical algorithm for the generation of thermal-change maps based on the phase of backscattered echo signals, as well as experimental results on tissue-like phantoms and pork loin. They also pointed out an important fundamental shortcoming of their method: the phase changes of the acoustic beam due to sound velocity variations occurring during tissue heating are not solely due to temperature effects on sound velocity but also due to the thermal expansion of the tissue (Karwat et al., 2016). Therefore, any thermal maps based on PSUE do not represent true temperature maps (or temperature difference maps), but rather maps of combined heat effects on tissue. Consequently, the method merely enables the visualization of local thermal fields generated by HIFU beams, which represents an intrinsic limitation when compared with MRT methods based on the water proton chemical shift.

An important consequence of this limitation is that PSUE cannot be used for real-time monitoring of tissue temperature under HIFU-induced heating; the HIFU "hot spot" can be localized but its actual temperature remains unknown. This is a major disadvantage as HIFU application cannot be controlled in real time as a function of the tissue temperature needed for ablation (the authors mentioned tumor ablation as an application of interest) (Karwat et al., 2016). Hence, the suggested technique exclusively serves the purpose of identifying the position of the HIFU beam before the actual HIFU treatment.

A further alternative to HIFU MRT, viz. temperature measurement with the help of thermochromic phantoms, is currently being developed by Eranki et al. (2019); see also Table S1. However, this approach was not meant to replace non-invasive *in vivo* thermometry; it was only intended to be used for technical characterization of HIFU devices and applications in environments where MRI or MRI-compatible HIFU equipment is unavailable. Another suggested application is the determination of absolute temperatures in phantoms, at sites located near the HIFU focus, for the purpose of modeling HIFU treatment. In this context it has been argued that the commonly used introduction of fiber optic or other temperature probes into the phantom may lead to inaccurate measurements as probes placed very close to the HIFU focus would interfere with the acoustic field. The "tissue-mimicking thermochromic phantom" (TMTCP) suggested is made of a gel that possesses the ability to change color permanently based on temperature. The thermochromic material in the gel was Magenta MB60°C concentrate (5% vol.). Calibrated color changes were compared with T_2 maps and phase PRFS-generated temperature change maps for TMTCP tubes in a 1.5-T magnet, following HIFU sonication. The tubes were then replaced by TMTCPs with patient-specific, 3D-printed anatomic structures for HIFU planning. The color intensity of the TMTCP decreased with temperature in a sigmoidal manner, notably for the green channel, with the inflection point at approximately 60°C–65°C. These values indicate the most sensitive temperature range for TMTCPs, the latter being most useful for the identification of regions expected to be at temperatures that induce tissue ablation at HIFU treatment. It is obvious that besides this narrow application, the TMTCP is unable to replace PRFS-based MRT.

Infrared thermography (IRT) has been used for medical imaging, as a diagnostic tool for multiple diseases. Combined with charged-coupled device (CCD) cameras, IRT serves as a screening tool for infections (Negishi et al., 2019) and has been widely used during the recent Covid-19 crisis. IRT was recently suggested by Cabizosu et al. for the evaluation and follow-up of muscular dystrophy (Cabizosu et al., 2019). Although IRT can be classified as an *in-vivo* thermometry method, it is unable to detect tissue temperature with the depth resolution needed for applications in hyperthermia and similar treatment modalities. This is because it only detects infrared radiation as emitted from the surface of an object. Consequently, CCD-IRT cannot be expected to replace MRT.

CONCLUSIONS AND OUTLOOK

The past years have seen significant improvements in contactless temperature measurement by magnetic resonance techniques as far as speed and accuracy/precision is concerned, and also increased versatility thanks to developments specifically dedicated to a continually expanding range of applications. This progress enabled better insight into details of thermal behavior of tissue and biomaterials. Although *in vivo* monitoring and controlling of thermotherapy procedures remain the principal domain of contactless MR thermometry, close observation of heat exchange processes in hydrogel-based biomaterials is also facilitated by these developments, and both domains benefit from the most recent approaches toward statistical quantification of thermal heterogeneity. This also applies to particular *ex-vivo* applications such as monitoring the cooling and re-warming of transplantation organs before and after storage, respectively. Although all new advances reported in this review have demonstrated their feasibility at the proof-of-principle stage, many of these have yet to prove their robustness and practicality in everyday routine applications.

In view of past practical experience with magnetic resonance-based thermometry, it is to be expected that many if not most of the recent advancements will indeed turn out to be valuable in various fields of applied research as well as in the clinic. In particular, hyperthermia treatment can be expected to benefit from the increase of speed and precision in PRF, although some of the most recent developments have yet to be integrated in routine protocols. In the future, more emphasis should be put on seamless data transfer between advanced PRF imaging and hyperthermia control, for which computers with very fast data processing are needed. This is imperative for optimal real-time control of hyperthermia through precise targeting of the body region to be irradiated and through instantaneous adjustment of heating power and/or localization as a function of rapidly changing tissue temperature. Such developments have made enormous progress for US-based hyperthermia but should also be accelerated for timely implementation in LITT, RF, and MW-based treatment regimes.

By contrast, the intrinsically slower MRS-based thermometry method is unlikely to become part of routine hyperthermia protocols. Its role will probably be confined to more specialized applications where knowledge of absolute temperature is more important than highest spatial resolution and speed. Newest developments have convincingly demonstrated that MRS-based temperature measurement is able to achieve both very high accuracy and precision when performed under optimized conditions. Further effort should be directed toward the exploration of the new, promising technique of quantitative statistical temperature distribution analysis based on MRS thermometry. Since this particular approach is very recent, no significant experience with *in vivo* applications is available at present. It is to be desired that future work be conducted in order to determine to what extent this novel method will be able to provide valuable insight into biological processes and to play a significant role in medical procedures and materials science.

SUPPLEMENTAL INFORMATION

Supplemental Information can be found online at https://doi.org/10.1016/j.isci.2020.101561.

ACKNOWLEDGMENTS

Support from Centre National de la Recherche Scientifique (UMR 7339) is gratefully acknowledged.

REFERENCES

Abraham, C.B., Loree-Spacek, J., Andrew Drainville, R., Pichardo, S., and Curiel, L. (2018). Development of custom RF coils for use in a small animal platform for magnetic resonance-guided focused ultrasound hyperthermia compatible with a clinical MRI scanner. Int. J. Hyperthermia *35*, 348–360.

Adams, M.S., Salgaonkar, V.A., Plata-Camargo, J., Jones, P.D., Pascal-Tenorio, A., Chen, H.-Y., Bouley, D.M., Sommer, G., Pauly, K.B., and Diederich, C.J. (2016). Endoluminal ultrasound applicators for MR-guided thermal ablation of pancreatic tumors: preliminary design and evaluation in a porcine pancreas model. Med. Phys. *43*, 4184.

Ahmed, E.M. (2015). Hydrogel: preparation, characterization, and applications: a review. J. Adv. Res. *6*, 105–121.

Aime, S., Botta, M., Fasano, M., Terreno, E., Kinchesh, P., Calabi, L., and Paleari, L. (1996). A new ytterbium chelate as contrast agent in chemical shift imaging and temperature sensitive probe for MR spectroscopy. Magn. Reson. Med. *35*, 648–651.

Aklan, B., Zilles, B., Paprottka, P., Manz, K., Pfirrmann, M., Santl, M., Abdel-Rahman, S., and Lindner, L.H. (2019). Regional deep hyperthermia: quantitative evaluation of predicted and direct measured temperature distributions in patients with high-risk extremity soft-tissue sarcoma. Int. J. Hyperthermia *36*, 170–185.

Andrews, M.D. (2004). Cryosurgery for common skin conditions. Am. Fam. Physician *69*, 2365–2372.

Arthurs, O.J., Graves, M.J., Edwards, A.D., Joubert, I., Set, P.A.K., and Lomas, D.J. (2014). Interactive neonatal gastrointestinal magnetic resonance imaging using fruit juice as an oral contrast media. BMC Med. Imaging *14*, 33.

Barnes, B. (1989). Freeze avoidance in a mammal: body temperatures below 0 degree C in an Arctic hibernator. Science *244*, 1593–1595.

Baust, J.G., Gage, A.A., Bjerklund Johansen, T.E., and Baust, J.M. (2014). Mechanisms of cryoablation: clinical consequences on malignant tumors. Cryobiology *68*, 1–11.

Bazrafshan, B., Koujan, A., Hübner, F., Leithäuser, C., Siedow, N., and Vogl, T.J. (2019). A thermometry software tool for monitoring laser-induced interstitial thermotherapy. Biomed. Tech. *64*, 449–457.

Bing, C., Cheng, B., Staruch, R.M., Nofiele, J., Wodzak Staruch, M., Szczepanski, D., Farrow-Gillespie, A., Yang, A., Laetsch, T.W., and Chopra, R. (2019). Breath-hold MR-HIFU hyperthermia: phantom and in vivo feasibility. Int. J. Hyperthermia *36*, 1084–1097.

Bing, C., Nofiele, J., Staruch, R., Ladouceur-Wodzak, M., Chatzinoff, Y., Ranjan, A., and Chopra, R. (2015). Localised hyperthermia in rodent models using an MRI-compatible high-intensity focused ultrasound system. Int. J. Hyperthermia *31*, 813–822.

Bing, C., Staruch, R.M., Tillander, M., Köhler, M.O., Mougenot, C., Ylihautala, M., Laetsch, T.W., and Chopra, R. (2016). Drift correction for accurate PRF-shift MR thermometry during mild hyperthermia treatments with MR-HIFU. Int. J. Hyperthermia *32*, 673–687.

Bloembergen, N., Purcell, E.M., and Pound, R.V. (1948). Relaxation effects in nuclear magnetic resonance absorption. Phys. Rev. *73*, 679–712.

Cabizosu, A., Carboni, N., Figus, A., Vegara-Meseguer, J.M., Casu, G., Hernández Jiménez, P., and Martinez-Almagro Andreo, A. (2019). Is infrared thermography (IRT) a possible tool for the evaluation and follow up of Emery-Dreifuss muscular dystrophy? A preliminary study. Med. Hypotheses *127*, 91–96.

Celicanin, Z., Manasseh, G., Petrusca, L., Scheffler, K., Auboiroux, V., Crowe, L.A., Hyacinthe, J.-N., Natsuaki, Y., Santini, F., Becker, C.D., et al. (2018). Hybrid ultrasound-MR guided HIFU treatment method with 3D motion compensation. Magn. Reson. Med. *79*, 2511–2523.

Chen, Q., Li, Y., Jiang, R., Zou, C., Tie, C., Wen, J., Yang, X., Zhang, X., Liu, X., and Zheng, H. (2020). A flexible 9-channel coil array for fast 3D MR thermometry in MR-guided high-intensity focused ultrasound (HIFU) studies on rabbits at 3 T. Magn. Reson. Imaging *65*, 37–44.

Chen, Y., Ge, M., Ali, R., Jiang, H., Huang, X., and Qiu, B. (2018). Quantitative MR thermometry based on phase-drift correction PRF shift method at 0.35 T. Biomed. Eng. Online *17*, 39.

Chesterton, L.S., Foster, N.E., and Ross, L. (2002). Skin temperature response to cryotherapy. Arch. Phys. Med. Rehabil. *83*, 543–549.

Cho, Z.H., Kim, D.J., and Kim, Y.K. (1988). Total inhomogeneity correction including chemical shifts and susceptibility by view angle tilting. Med. Phys. *15*, 7–11.

Chu, W., Staruch, R.M., Pichardo, S., Tillander, M., Köhler, M.O., Huang, Y., Ylihautala, M., McGuffin, M., Czarnota, G., and Hynynen, K. (2016). Magnetic resonance-guided high-intensity focused ultrasound hyperthermia for recurrent rectal cancer: MR thermometry evaluation and preclinical validation. Int. J. Radiat. Oncol. Biol. Phys. *95*, 1259–1267.

Ciris, P.A., Cheng, C.-C., Mei, C.-S., Panych, L.P., and Madore, B. (2017). Dual-Pathway sequences for MR thermometry: when and where to use them. Magn. Reson. Med. *77*, 1193–1200.

Clebak, K.T., Mendez-Miller, M., and Croad, J. (2020). Cutaneous cryosurgery for common skin conditions. Am. Fam. Physician *101*, 399–406.

Colen, R.R., Sahnoune, I., and Weinberg, J.S. (2017). Neurosurgical applications of high-intensity focused ultrasound with magnetic resonance thermometry. Neurosurg. Clin. N. Am. *28*, 559–567.

Coman, D., Trubel, H.K., Rycyna, R.E., and Hyder, F. (2009). Brain temperature and pH measured by (1)H chemical shift imaging of a thulium agent. NMR Biomed. *22*, 229–239.

Cornud, F., Bomers, J., Futterer, J.J., Ghai, S., Reijnen, J.S., and Tempany, C. (2018). MR imaging-guided prostate interventional imaging: ready for a clinical use? Diagn. Interv. Imaging *99*, 743–753.

Crake, C., Meral, F.C., Burgess, M.T., Papademetriou, I.T., McDannold, N.J., and Porter, T.M. (2017). Combined passive acoustic mapping and magnetic resonance thermometry for monitoring phase-shift nanoemulsion enhanced focused ultrasound therapy. Phys. Med. Biol. *62*, 6144–6163.

Crake, C., Papademetriou, I.T., Zhang, Y., Vykhodtseva, N., McDannold, N.J., and Porter, T.M. (2018). Simultaneous passive acoustic mapping and magnetic resonance thermometry for monitoring of cavitation-enhanced tumor ablation in rabbits using focused ultrasound and phase-shift nanoemulsions. Ultrasound Med. Biol. *44*, 2609–2624.

Cressman, E.N.K., and Guo, C. (2018). First in vivo test of thermoembolization: turning tissue against itself using transcatheter chemistry in a porcine model. Cardiovasc. Intervent. Radiol. *41*, 1611–1617.

Curto, S., Aklan, B., Mulder, T., Mils, O., Schmidt, M., Lamprecht, U., Peller, M., Wessalowski, R., Lindner, L.H., Fietkau, R., et al. (2019). Quantitative, multi-institutional evaluation of MR thermometry accuracy for deep-pelvic MR-hyperthermia systems operating in multi-vendor MR-systems using a new anthropomorphic phantom. Cancers *11*, 1709.

Curto, S., Faridi, P., Shrestha, T.B., Pyle, M., Maurmann, L., Troyer, D., Bossmann, S.H., and Prakash, P. (2018). An integrated platform for small-animal hyperthermia investigations under ultra-high-field MRI guidance. Int. J. Hyperthermia *34*, 341–351.

Davis, R.M., and Warren, W.S. (2015). Intermolecular zero quantum coherences enable accurate temperature imaging in red bone marrow. Magn. Reson. Med. *74*, 63–70.

Davis, R.M., Zhou, Z., Chung, H., and Warren, W.S. (2016). Multi-spin echo spatial encoding provides three-fold improvement of temperature precision during intermolecular zero quantum thermometry. Magn. Reson. Med. *75*, 1958–1966.

Denis de Senneville, B., Quesson, B., and Moonen, C.T.W. (2005). Magnetic resonance temperature imaging. Int. J. Hyperthermia *21*, 515–531.

Eranki, A., Mikhail, A.S., Negussie, A.H., Katti, P.S., Wood, B.J., and Partanen, A. (2019). Tissue-mimicking thermochromic phantom for characterization of HIFU devices and applications. Int. J. Hyperthermia *36*, 518–529.

Ertürk, M.A., Sathyanarayana Hegde, S., and Bottomley, P.A. (2016). Radiofrequency ablation, MR thermometry, and high-spatial-resolution MR parametric imaging with a single, minimally invasive device. Radiology *281*, 927–932.

Fahrenholtz, S.J., Guo, C., MacLellan, C.J., Yung, J.P., Hwang, K.-P., Layman, R.R., Stafford, R.J., and Cressman, E. (2019). Temperature mapping of exothermic in situ chemistry: imaging of thermoembolization via MR. Int. J. Hyperthermia *36*, 730–738.

Fauci, A. (2008). Harrison's Principles of Internal Medicine, Seventeenth Edition. (McGraw-Hill).

Ferrer, C.J., Bartels, L.W., van der Velden, T.A., Grüll, H., Heijman, E., Moonen, C.T.W., and Bos, C. (2020). Field drift correction of proton resonance frequency shift temperature mapping with multichannel fast alternating nonselective free induction decay readouts. Magn. Reson. Med. *83*, 962–973.

Ferrer, C.J., Bartels, L.W., van Stralen, M., Denis de Senneville, B., Moonen, C.T.W., and Bos, C. (2018). Fluid filling of the digestive tract for improved proton resonance frequency shift-based MR thermometry in the pancreas. J. Magn. Reson. Imaging *47*, 692–701.

Galiana, G., Branca, R.T., Jenista, E.R., and Warren, W.S. (2008). Accurate temperature imaging based on intermolecular coherences in magnetic resonance. Science *322*, 421–424.

Geoghegan, R., Santamaria, A., Priester, A., Zhang, L., Wu, H., Grundfest, W., Marks, L., and Natarajan, S. (2019). A tissue-mimicking prostate phantom for 980 nm laser interstitial thermal therapy. Int. J. Hyperthermia *36*, 993–1002.

Gorny, K.R., Favazza, C.P., Lu, A., Felmlee, J.P., Hangiandreou, N.J., Browne, J.E., Stenzel, W.S., Muggli, J.L., Anderson, A.G., Thompson, S.M., and Woodrum, D.A. (2019). Practical implementation of robust MR-thermometry during clinical MR-guided microwave ablations in the liver at 1.5 T. Phys. Med. *67*, 91–99.

Graedel, N.N., McNab, J.A., Chiew, M., and Miller, K.L. (2017). Motion correction for functional MRI with three-dimensional hybrid radial-Cartesian EPI. Magn. Reson. Med. *78*, 527–540.

Grüll, H., and Langereis, S. (2012). Hyperthermia-triggered drug delivery from temperature-sensitive liposomes using MRI-guided high intensity focused ultrasound. J. Control. Release *161*, 317–327.

Haacke, E.M., Brown, R.W., Thompson, M.R., and Venkatesan, R. (1999). Magnetic Resonance Imaging - Physical Principles and Sequence Design (Wiley-Liss).

Hahn, E.L. (1950). Spin echoes. Phys. Rev. *80*, 580–594.

Hartmann, J., Gellermann, J., Brandt, T., Schmidt, M., Pyatykh, S., Hesser, J., Ott, O., Fietkau, R., and Bert, C. (2017). Optimization of single voxel MR spectroscopy sequence parameters and data analysis methods for thermometry in deep hyperthermia treatments. Technol. Cancer Res. Treat. *16*, 470–481.

Heyn, C.C., Bishop, J., Duffin, K., Lee, W., Dazai, J., Spring, S., Nieman, B.J., and Sled, J.G. (2017). Magnetic resonance thermometry of flowing blood. NMR Biomed. *30*, e3772.

Hofstetter, L.W., Yeo, D.T.B., Dixon, W.T., Kempf, J.G., Davis, C.E., and Foo, T.K. (2012). Fat-referenced MR thermometry in the breast and prostate using IDEAL. J. Magn. Reson. Imaging *36*, 722–732.

Hübner, F., Leithäuser, C., Bazrafshan, B., Siedow, N., and Vogl, T.J. (2017). Validation of a mathematical model for laser-induced thermotherapy in liver tissue. Lasers Med. Sci. *32*, 1399–1409.

Ishihara, Y., Calderon, A., Watanabe, H., Okamoto, K., Suzuki, Y., Kuroda, K., and Suzuki, Y. (1995). A precise and fast temperature mapping using water proton chemical shift. Magn. Reson. Med. *34*, 814–823.

Jenista, E.R., Galiana, G., Branca, R.T., Yarmolenko, P.S., Stokes, A.M., Dewhirst, M.W., and Warren, W.S. (2010). Application of mixed spin iMQCs for temperature and chemical-selective imaging. J. Magn. Reson. *204*, 208–218.

Jermakowicz, W.J., Mahavadi, A.K., Cajigas, I., Dan, L., Guerra, S., Farooq, G., Shah, A.H., D'Haese, P.F., Ivan, M.E., Jagid, J.R., and Komotar, R.J. (2019). Predictive modeling of brain tumor laser ablation dynamics. J. Neurooncol. *144*, 193–203.

Jessen, C. (2001). Temperature Regulation in Humans and Other Mammals (Springer).

Jonathan, S.V., and Grissom, W.A. (2018). Volumetric MRI thermometry using a three-dimensional stack-of-stars echo-planar imaging pulse sequence. Magn. Reson. Med. *79*, 2003–2013.

Karwat, P., Kujawska, T., Lewin, P.A., Secomski, W., Gambin, B., and Litniewski, J. (2016). Determining temperature distribution in tissue in the focal plane of the high (>100 W/cm(2)) intensity focused ultrasound beam using phase shift of ultrasound echoes. Ultrasonics *65*, 211–219.

Kim, K., Breton, E., Gangi, A., and Vappou, J. (2020). Simultaneous fat-referenced proton resonance frequency shift thermometry and MR elastography for the monitoring of thermal ablations. Magn. Reson. Med. *84*, 339–347.

Kuroda, K., Oshio, K., Chung, A.H., Hynynen, K., and Jolesz, F.A. (1997). Temperature mapping using the water proton chemical shift: a chemical shift selective phase mapping method. Magn. Reson. Med. *38*, 845–851.

Lechner-Greite, S.M., Hehn, N., Werner, B., Zadicario, E., Tarasek, M., and Yeo, D. (2016). Minimizing eddy currents induced in the ground plane of a large phased-array ultrasound applicator for echo-planar imaging-based MR thermometry. J. Ther. Ultrasound *4*, 4.

Lipsman, N., Schwartz, M.L., Huang, Y., Lee, L., Sankar, T., Chapman, M., Hynynen, K., and Lozano, A.M. (2013). MR-guided focused ultrasound thalamotomy for essential tremor: a proof-of-concept study. Lancet Neurol. *12*, 462–468.

Liu, G., Qin, Q., Chan, K.W., Li, Y., Bulte, J.W., McMahon, M.T., van Zijl, P.C., and Gilad, A.A. (2014). Non-invasive temperature mapping using temperature-responsive water saturation shift referencing (T-WASSR) MRI. NMR Biomed. *27*, 320–331.

Lorton, O., Guillemin, P.C., Mori, N., Crowe, L.A., Boudabbous, S., Terraz, S., Becker, C.D., Cattin, P., Salomir, R., and Gui, L. (2019). Self-scanned HIFU ablation of moving tissue using real-time hybrid US-MR imaging. IEEE Trans. Biomed. Eng. *66*, 2182–2191.

Lutz, N.W., and Bernard, M. (2019a). A method for multiparametric statistical quantification of the heterogeneity of free Na(+) concentration by (19) F MR spectroscopy: proof of principle in silico and in vitro. NMR Biomed. *32*, e4117.

Lutz, N.W., and Bernard, M. (2019b). Multiparametric statistical quantification of pH heterogeneity by (1) H MRS and MRSI of extracellular pH markers: proof of principle. NMR Biomed. *32*, e4134.

Lutz, N.W., and Bernard, M. (2018a). Thermal heterogeneity within aqueous materials quantified by (1)H NMR spectroscopy: multiparametric validation in silico and in vitro. J. Magn. Reson. *287*, 56–64.

Lutz, N.W., and Bernard, M. (2018b). Multiparametric quantification of heterogeneity of metal ion concentrations, as demonstrated for [Mg2+] by way of 31P MRS. J. Magn. Reson. *294*, 71–82.

Lutz, N.W., and Bernard, M. (2018c). Multiparametric quantification of the heterogeneity of free Ca2+ concentration by 19F MR spectroscopy. J. Magn. Reson. *297*, 96–107.

Lutz, N.W., and Bernard, M. (2017). Multiparametric quantification of thermal heterogeneity within aqueous materials by water 1H NMR spectroscopy: paradigms and algorithms. PLoS One *12*, e0178431.

Lutz, N.W., Kuesel, A.C., and Hull, W.E. (1993). A 1H-NMR method for determining temperature in cell culture perfusion systems. Magn. Reson. Med. *29*, 113–118.

Lutz, N.W., Le Fur, Y., Chiche, J., Pouyssegur, J., and Cozzone, P.J. (2013). Quantitative in-vivo characterization of intracellular and extracellular pH profiles in heterogeneous tumors: a novel method enabling multiparametric pH analysis. Cancer Res. *73*, 4616–4628.

MacDonell, J., Patel, N., Rubino, S., Ghoshal, G., Fischer, G., Burdette, E.C., Hwang, R., and Pilitsis, J.G. (2018). Magnetic resonance-guided interstitial high-intensity focused ultrasound for brain tumor ablation. Neurosurg. Focus *44*, E11.

Madigan, M.T., Bender, K.S., Buckley, D.H., Sattley, W.M., and Stahl, D.A. (2018). Brock Biology of Microorganisms, Fifteenth Edition. (Pearson).

Madore, B., Panych, L.P., Mei, C.-S., Yuan, J., and Chu, R. (2011). Multipathway sequences for MR thermometry. Magn. Reson. Med. *66*, 658–668.

Mantha, S., Pillai, S., Khayambashi, P., Upadhyay, A., Zhang, Y., Tao, O., Pham, H.M., and Tran, S.D. (2019). Smart hydrogels in tissue engineering and regenerative medicine. Materials *12*, 3323.

Maudsley, A.A., Goryawala, M.Z., and Sheriff, S. (2017). Effects of tissue susceptibility on brain temperature mapping. Neuroimage *146*, 1093–1101.

McVicar, N., Li, A.X., Suchý, M., Hudson, R.H.E., Menon, R.S., and Bartha, R. (2013). Simultaneous in vivo pH and temperature mapping using a PARACEST-MRI contrast agent. Magn. Reson. Med. *70*, 1016–1025.

Mei, J., Riedel, N., Grittner, U., Endres, M., Banneke, S., and Emmrich, J.V. (2018). Body temperature measurement in mice during acute illness: implantable temperature transponder versus surface infrared thermometry. Sci. Rep. *8*, 3526.

Michel, S.G., LaMuraglia Ii, G.M., Madariaga, M.L.L., and Anderson, L.M. (2015). Innovative cold storage of donor organs using the Paragonix Sherpa Pak devices. Heart Lung Vessel. *7*, 246–255.

Mintzopoulos, D., Ratai, E.-M., He, J., Gonzalez, R.G., and Kaufman, M.J. (2019). Simian immunodeficiency virus transiently increases brain temperature in rhesus monkeys: detection with magnetic resonance spectroscopy thermometry. Magn. Reson. Med. *81*, 2896–2904.

Mitchell, D., Fahrenholtz, S., MacLellan, C., Bastos, D., Rao, G., Prabhu, S., Weinberg, J., Hazle, J., Stafford, J., and Fuentes, D. (2018). A heterogeneous tissue model for treatment planning for magnetic resonance-guided laser interstitial thermal therapy. Int. J. Hyperthermia *34*, 943–952.

Mueller, P., and Adam, A. (2012). Interventional Oncology (Springer).

Mukherjee, R.K., Roujol, S., Chubb, H., Harrison, J., Williams, S., Whitaker, J., O'Neill, L., Silberbauer, J., Neji, R., Schneider, R., et al. (2018). Epicardial electroanatomical mapping, radiofrequency ablation, and lesion imaging in the porcine left ventricle under real-time magnetic resonance imaging guidance-an in vivo feasibility study. Europace *20*, f254–f262.

Mulder, H.T., Curto, S., Paulides, M.M., Franckena, M., and van Rhoon, G.C. (2018). Systematic quality assurance of the BSD2000-3D MR-compatible hyperthermia applicator performance using MR temperature imaging. Int. J. Hyperthermia *35*, 305–313.

Munier, S.M., Desai, A.N., Patel, N.V., and Danish, S.F. (2020). Effects of intraoperative magnetic

resonance thermal imaging signal artifact during laser interstitial thermal therapy on thermal damage estimate and postoperative magnetic resonance imaging ablative area concordance. Oper. Neurosurg. *18*, 524–530.

Negishi, T., Sun, G., Sato, S., Liu, H., Matsui, T., Abe, S., Nishimura, H., and Kirimoto, T. (2019). Infection screening system using thermography and CCD camera with good stability and swiftness for non-contact vital-signs measurement by feature matching and MUSIC algorithm. Conf. Proc. IEEE Eng. Med. Biol. Soc. *2019*, 3183–3186.

Odéen, H., and Parker, D.L. (2019a). Magnetic resonance thermometry and its biological applications - physical principles and practical considerations. Prog. Nucl. Magn. Reson. Spectrosc. *110*, 34–61.

Odéen, H., and Parker, D.L. (2019b). Improved MR thermometry for laser interstitial thermotherapy. Lasers Surg. Med. *51*, 286–300.

Ozenne, V., Constans, C., Bour, P., Santin, M.D., Valabrègue, R., Ahnine, H., Pouget, P., Lehéricy, S., Aubry, J.-F., and Quesson, B. (2020). MRI monitoring of temperature and displacement for transcranial focus ultrasound applications. Neuroimage *204*, 116236.

Ozenne, V., Toupin, S., Bour, P., de Senneville, B.D., Lepetit-Coiffé, M., Boissenin, M., Benois-Pineau, J., Hansen, M.S., Inati, S.J., Govari, A., et al. (2017). Improved cardiac magnetic resonance thermometry and dosimetry for monitoring lesion formation during catheter ablation. Magn. Reson. Med. *77*, 673–683.

Ozhinsky, E., Salgaonkar, V.A., Diederich, C.J., and Rieke, V. (2018). MR thermometry-guided ultrasound hyperthermia of user-defined regions using the ExAblate prostate ablation array. J. Ther. Ultrasound *6*, 7.

Panikov, N.S., Flanagan, P.W., Oechel, W.C., Mastepanov, M.A., and Christensen, T.R. (2006). Microbial activity in soils frozen to below −39°C. Soil Biol. Biochem. *38*, 785–794.

Parmala, M., Eriksson, M., Rytioja, M., Tanttu, J., and Köhler, M. (2016). Temperature measurement in human fat with T2 imaging. J. Magn. Reson. Imaging *43*, 1171–1178.

Petrusca, L., Viallon, M., Terraz, S., de Luca, V., Celicanin, Z., Auboiroux, V., Brunke, S., Cattin, P., and Salomir, R. (2012). Simultaneous ultrasound imaging and MRI acquisition. In Interventional Magnetic Resonance Imaging, T. Kahn and H. Busse, eds. (Springer-Verlag), pp. 289–302.

Piazena, H., Muller, W., Pendl, W., von Ah, S., Cap, V.H., Hug, P.J., Sidler, X., Pluschke, G., and Vaupel, P. (2019). Thermal field formation during wIRA-hyperthermia: temperature measurements in skin and subcutis of piglets as a basis for thermotherapy of superficial tumors and local skin infections caused by thermosensitive microbial pathogens. Int. J. Hyperthermia *36*, 938–952.

Proctor, W.G., and Yu, F.C. (1950). The dependence of a nuclear magnetic resonance frequency upon chemical compound. Phys. Rev. *77*, 717.

Rango, M., Bonifati, C., and Bresolin, N. (2015). Post-activation brain warming: a 1-H MRS thermometry study. PLoS One *10*, e0127314.

Rieke, V., and Butts Pauly, K. (2008). MR thermometry. J. Magn. Reson. Imaging *27*, 376–390.

Saad, H., and Aladawy, M. (2013). Temperature management in cardiac surgery. Glob. Cardiol. Sci. Pract. *2013*, 44–62.

Sarhan, M.A.A., and Alamrri, S. (2014). Characterization and identification of moderately thermophilic bacteria isolated from jazan hot springs in Saudi arabia. Egypt. Acad. J. Biol. Sci. *6*, 67–75.

Savina, I.N., Ingavle, G.C., Cundy, A.B., and Mikhalovsky, S.V. (2016). A simple method for the production of large volume 3D macroporous hydrogels for advanced biotechnological, medical and environmental applications. Sci. Rep. *6*, 21154.

Schreurs, T.J.L., van Gorkum, R., Zhang, X.U., Faber, D.J., van Leeuwen, T.G., Nicolay, K., and Strijkers, G.J. (2017). Noninvasive fluence rate mapping in living tissues using magnetic resonance thermometry. J. Biomed. Opt. *22*, 36001.

Siedek, F., Yeo, S.Y., Heijman, E., Grinstein, O., Bratke, G., Heneweer, C., Puesken, M., Persigehl, T., Maintz, D., and Grüll, H. (2019a). Magnetic resonance-guided high-intensity focused ultrasound (MR-HIFU): overview of emerging applications (Part 2). Röfo *191*, 531–539.

Siedek, F., Yeo, S.Y., Heijman, E., Grinstein, O., Bratke, G., Heneweer, C., Puesken, M., Persigehl, T., Maintz, D., and Grüll, H. (2019b). Magnetic resonance-guided high-intensity focused ultrasound (MR-HIFU): technical background and overview of current clinical applications (Part 1). Röfo *191*, 522–530.

Staruch, R.M., Hynynen, K., and Chopra, R. (2015). Hyperthermia-mediated doxorubicin release from thermosensitive liposomes using MR-HIFU: therapeutic effect in rabbit Vx2 tumours. Int. J. Hyperthermia *31*, 118–133.

Takai, K., Nakamura, K., Toki, T., Tsunogai, U., Miyazaki, M., Miyazaki, J., Hirayama, H., Nakagawa, S., Nunoura, T., and Horikoshi, K. (2008). Cell proliferation at 122 degrees C and isotopically heavy CH4 production by a hyperthermophilic methanogen under high-pressure cultivation. Proc. Natl. Acad. Sci. U S A *105*, 10949–10954.

Tan, J., Mougenot, C., Pichardo, S., Drake, J.M., and Waspe, A.C. (2019). Motion compensation using principal component analysis and projection onto dipole fields for abdominal magnetic resonance thermometry. Magn. Reson. Med. *81*, 195–207.

Tanner, C., Zur, Y., French, K., Samei, G., Strehlow, J., Sat, G., McLeod, H., Houston, G., Kozerke, S., Székely, G., et al. (2016). In vivo validation of spatio-temporal liver motion prediction from motion tracked on MR thermometry images. Int. J. Comput. Assist. Radiol. Surg. *11*, 1143–1152.

Tillander, M., Hokland, S., Koskela, J., Dam, H., Andersen, N.P., Pedersen, M., Tanderup, K., Ylihautala, M., and Köhler, M. (2016). High intensity focused ultrasound induced in vivo large volume hyperthermia under 3D MRI temperature control. Med. Phys. *43*, 1539–1549.

Tong, G., von Garlen, N.N.A., Wowro, S.J., Lam, P.D., Krech, J., Berger, F., and Schmitt, K.R.L. (2019). Post-TTM rebound pyrexia after ischemia-reperfusion injury results in sterile inflammation and apoptosis in cardiomyocytes. Mediators Inflamm. *2019*, 6431957.

Untenberger, M., Tan, Z., Voit, D., Joseph, A.A., Roeloffs, V., Merboldt, K.D., Schätz, S., and Frahm, J. (2016). Advances in real-time phase-contrast flow MRI using asymmetric radial gradient echoes. Magn. Reson. Med. *75*, 1901–1908.

Verius, M., Frank, F., Gizewski, E., and Broessner, G. (2019). Magnetic resonance spectroscopy thermometry at 3 tesla: importance of calibration measurements. Ther. Hypothermia Temp. Manag. *9*, 146–155.

Vescovo, E., Levick, A., Childs, C., Machin, G., Zhao, S., and Williams, S.R. (2013). High-precision calibration of MRS thermometry using validated temperature standards: effects of ionic strength and protein content on the calibration. NMR Biomed. *26*, 213–223.

Warren, D.S., Sutherland, S.P.H., Kao, J.Y., Weal, G.R., and Mackay, S.M. (2017). The preparation and simple analysis of a clay nanoparticle composite hydrogel. J. Chem. Educ. *94*, 1772–1779.

Warriner, K., Hay, J., Crean, C., de Namor, A.F.D., Narayan, R., Mills, A., Gilmartin, N., Jur, J., Reddy, S.M., and Thompson, M. (2014). Advanced Synthetic Materials in Detection Science (Royal Society of Chemistry).

Weber, H., Taviani, V., Yoon, D., Ghanouni, P., Pauly, K.B., and Hargreaves, B.A. (2017). MR thermometry near metallic devices using multispectral imaging. Magn. Reson. Med. *77*, 1162–1169.

Wermter, F.C., Mitschke, N., Bock, C., and Dreher, W. (2017). Temperature dependence of (1)H NMR chemical shifts and its influence on estimated metabolite concentrations. MAGMA *30*, 579–590.

Winter, L., Oberacker, E., Paul, K., Ji, Y., Oezerdem, C., Ghadjar, P., Thieme, A., Budach, V., Wust, P., and Niendorf, T. (2016). Magnetic resonance thermometry: methodology, pitfalls and practical solutions. Int. J. Hyperthermia *32*, 63–75.

Winter, L., Ozerdem, C., Hoffmann, W., Santoro, D., Muller, A., Waiczies, H., Seemann, R., Graessl, A., Wust, P., and Niendorf, T. (2013). Design and evaluation of a hybrid radiofrequency applicator for magnetic resonance imaging and RF induced hyperthermia: electromagnetic field simulations up to 14.0 Tesla and proof-of-concept at 7.0 Tesla. PLoS One *8*, e61661.

Yuan, J., Mei, C.-S., Panych, L.P., McDannold, N.J., and Madore, B. (2012). Towards fast and accurate temperature mapping with proton resonance frequency-based MR thermometry. Quant. Imaging Med. Surg. *2*, 21–32.

Zachiu, C., Ries, M., Moonen, C., and de Senneville, B.D. (2017). An adaptive non-local-means filter for real-time MR-thermometry. IEEE Trans. Med. Imaging *36*, 904–916.

Zhang, L., Armstrong, T., Li, X., and Wu, H.H. (2019). A variable flip angle golden-angle-ordered 3D stack-of-radial MRI technique for simultaneous proton resonant frequency shift and T(1) -based thermometry. Magn. Reson. Med. *82*, 2062–2076.

Zhang, Z., Michaelis, T., and Frahm, J. (2017). Towards MRI temperature mapping in real time-the proton resonance frequency method with undersampled radial MRI and nonlinear inverse reconstruction. Quant Imaging Med. Surg. *7*, 251–258.

Zhu, L., Partanen, A., Talcott, M.R., Gach, H.M., Greco, S.C., Henke, L.E., Contreras, J.A., Zoberi, I., Hallahan, D.E., Chen, H., and Altman, M.B. (2019). Feasibility and safety assessment of magnetic resonance-guided high-intensity focused ultrasound (MRgHIFU)-mediated mild hyperthermia in pelvic targets evaluated using an in vivo porcine model. Int. J. Hyperthermia *36*, 1147–1159.

Zhu, M., Sun, Z., and Ng, C.K. (2017). Image-guided thermal ablation with MR-based thermometry. Quant Imaging Med. Surg. *7*, 356–368.